University of Groningen

The nature of the ISM in galaxies during the star-formation activity peak of the Universe

Popping, G.; Pérez-Beaupuits, J. P.; Spaans, M.; Trager, S. C.; Somerville, R. S.

IMPORTANT NOTE: You are advised to consult the publisher's version (publisher's PDF) if you wish to cite from it. Please check the document version below.

Document Version
Publisher's PDF, also known as Version of record

Link to publication in University of Groningen/UMCG research database

The nature of the ISM in galaxies during the star-formation activity peak of the Universe

G. Popping,[1]★ J. P. Pérez-Beaupuits,[2] M. Spaans,[1] S. C. Trager[1] and R. S. Somerville[3]

[1]*Kapteyn Astronomical Institute, University of Groningen, Postbus 800, NL-9700 AV Groningen, the Netherlands*
[2]*Max-Planck-Institut für Radioastronomie, Auf dem Hügel 69, D-53121, Bonn, Germany*
[3]*Department of Physics and Astronomy, Rutgers University, 136 Frelinghuysen Road, Piscataway, NJ 08854, USA*

ABSTRACT

We combine a semi-analytic model of galaxy formation, tracking atomic and molecular phases of cold gas, with a three-dimensional radiative-transfer and line tracing code to study the sub-mm emission from atomic and molecular species (CO, HCN, [C I], [C II], [O I]) in galaxies. We compare the physics that drives the formation of stars at the epoch of peak star formation (SF) in the Universe ($z = 2.0$) with that in local galaxies. We find that normal star-forming galaxies at high redshift have much higher CO-excitation peaks than their local counterparts and that CO cooling takes place at higher excitation levels. CO line ratios increase with redshift as a function of galaxy star-formation rate, but are well correlated with H_2 surface density independent of redshift. We find an increase in the [O I]/[C II] line ratio in typical star-forming galaxies at $z = 1.2$ and $z = 2.0$ with respect to counterparts at $z = 0$. Our model results suggest that typical star-forming galaxies at high redshift consist of much denser and warmer star-forming clouds than their local counterparts. Galaxies belonging to the tail of the SF activity peak at $z = 1.2$ are already less dense and cooler than counterparts during the actual peak of SF activity ($z = 2.0$). We use our results to discuss how future ALMA surveys can best confront our predictions and constrain models of galaxy formation.

Key words: ISM: atoms – ISM: lines and bands – ISM: molecules – galaxies: evolution – galaxies: formation – galaxies: ISM.

1 INTRODUCTION

The star-formation rate density (SFRD) of the Universe peaked at redshifts $z \sim 1$–3 after which it gradually dropped towards its present-day value (e.g. Hopkins & Beacom 2006). This epoch marks a crucial period in the history of the Universe, when the bulk of stars in massive galaxies were likely formed.

The development of large samples of galaxies with extensive multi-wavelength information has been the first step in understanding the physical conditions under which these galaxies formed their stars. These surveys probe fundamental properties such as the stellar mass, star-formation rate (SFR) and sizes of these galaxies (e.g. *GOODS*, *COSMOS* and *CANDELS*; Giavalisco et al. 2004; Scoville et al. 2007; Grogin et al. 2011; Koekemoer et al. 2011). Information about the gas properties of these objects has largely been unavailable. Direct observations of the gaseous content of typical star-forming galaxies are only available for a few dozen objects (e.g. Daddi et al. 2010; Genzel et al. 2010; Tacconi et al. 2010, 2013; Geach et al. 2011; Bauermeister et al. 2013). These observations are usually limited to measures of the gaseous mass of galaxies, and do not probe the physical state under which the stars are formed: the local radiation field, temperature, and density of the gas are unknown. Some authors have addressed these characteristic properties of molecular (Dannerbauer et al. 2009; Danielson et al. 2011) and atomic gas (Walter et al. 2011), but such studies are limited to the most actively star-forming or submillimeter galaxies (SMGs), and are not representative of the bulk galaxy population (Walter et al. 2011). We refer the reader to Carilli & Walter (2013) for a full overview of observations of the interstellar medium (ISM) in high-z galaxies.

The temperature, density and turbulence of the gas and the local radiation field are the main characteristics in play during the formation of stars out of molecular clouds, as they set the free-fall time, pressure and sound speed of the gas. Furthermore, the gas contains several coolant species, responsible for the dominant cooling of the ISM. In order to fully understand the physics that drives the bulk of the SF during the peak in SFRD of the Universe, it is important to probe these gas properties in typical star-forming galaxies (i.e. responsible for the bulk of SF during the SF peak of the Universe) and to understand under which conditions stars formed. It is unclear if the physical state of the gas in these galaxies is similar to local

★ E-mail: g.popping@astro.rug.nl

counterparts or if the ISM physics that drives the SF efficiency is significantly different. A proper comparison of the density, pressure, temperature and radiation field of the star-forming gas in galaxies at $z \sim 2.0$ with local galaxies can shed light on the conditions under which galaxies formed their stars during the SF peak of the Universe with respect to the local Universe.

In the near future, millimeter telescopes such as ALMA (Atacama Large Millimeter Array), PdBI (Plateau du Bureau Interferometer), and LMT (Large Millimeter Telescope) will be able to observe multiple line transitions of tracers of molecular gas and atomic gas for statistical samples of high-redshift galaxies. These observations will not only reveal the physics under which star formation (SF) took place, but will also provide theorists with new constraints on the physical state of the star-forming cold gas. It is therefore important to develop computationally efficient methods to study the sub-mm line properties of the cold gas in cosmologically representative galaxy samples.

The chemical evolution of molecular species can be obtained by the modelling of Photon (UV) Dominated Regions (PDR) and X-ray dominated regions (XDR) (e.g. Meijerink, Spaans & Israel 2006, 2007). Besides UV and X-ray heating of the gas, cosmic rays and shocks can also add radiative or mechanical energy to the system, heat the gas and play a major role in the PDR and XDR chemistry (Loenen et al. 2008). Furthermore, radiative feedback on molecular clouds can also result in a PDR-dominated molecular chemistry. Large velocity gradient (LVG) radiative transfer codes (e.g. Weiß, Walter & Scoville 2005; Poelman & Spaans 2006; van der Tak et al. 2007) provide accurate estimates of line emission along the energy ladder of molecular and atomic species within PDRs. The LVG formalism permits the treatment of coupled radiative transfer and molecular excitation as a local problem. It assumes that the photons emitted from one region do not interact with molecules in other regions due to Doppler shift. Photons only interact with molecules in the local region where they were emitted. These methods have proven to be excellent theoretical tools to reproduce the sub-mm line emission of various chemical species in molecular clouds, ranging over a large variety of densities and temperatures. They do not necessarily encompass the large variety of gaseous phases in a galaxy's ISM, and the LVG assumption that photons do not interact with molecules in other regions may not necessarily be true. A proper comparison between theory and observations of galaxies therefore requires PDR and radiative transfer methods to be embedded within cosmological models of galaxy formation and evolution. It furthermore requires one to properly calculate the interaction of photons (escape probability) throughout all the grid cells along the line of sight, taking into account the opacities at each velocity (or frequency) resolution element.

In the last decade large efforts have been made to develop numerical models in a cosmological context to understand the relation between dense and cold gas properties and other galaxy properties (e.g. Pelupessy, Papadopoulos & van der Werf 2006; Narayanan et al. 2008; Robertson & Kravtsov 2008; Gnedin, Tassis & Kravtsov 2009; Wada, Papadopoulos & Spaans 2009; Christensen et al. 2012; Kuhlen et al. 2012). Only occasionally have these efforts been combined with detailed modelling of the sub-mm line intensity coming from chemical species such as CO, [C II] and HCN (Narayanan et al. 2008; Pérez-Beaupuits, Wada & Spaans 2011).

Semi-analytic models provide an alternative approach to the modelling of galaxy formation within the framework of a Λ-cold dark matter cosmology. Simplified but physically motivated recipes are used to track the cooling of hot gas into galaxies, the radial size of discs, the formation of stars, the energy input from supernovae

(SNe) and active galactic nuclei (AGN) into the ISM. The latest generation of models explicitly includes the detailed tracking of the atomic and molecular hydrogen content of galaxies and a more physically motivated H_2-based SF recipe (Fu et al. 2010; Lagos et al. 2011a,b; Krumholz & Dekel 2012; Fu et al. 2012; Popping, Somerville & Trager 2014, Somerville, Popping & Trager, in preparation). These models have proven to be successful in reproducing the available observational estimates of the overall H I and H_2 properties of local and high-redshift galaxies, such as H I and H_2 mass, the size–stellar mass relation of galaxies, H I and H_2 mass function, the sizes of H I discs in the nearby Universe and the observed size evolution of star-forming discs. Although very useful in shaping our understanding of galaxy evolution, they do not provide directly observable predictions of detailed properties of the cold gas in discs such as temperature and density. A first attempt to model the CO line emission of galaxies over a wide range of galaxy properties was made by Lagos et al. (2012). The authors did not focus on other sub-mm emission lines.

In this paper we present new predictions of sub-mm line intensities for galaxies selected from a semi-analytic model of galaxy formation. We focus on CO line transitions, HCN, [C II] 158 μm, [O I] 63 μm, and the carbon fine structure lines (CI($^3P_1 \rightarrow {}^3P_0$) and CI($^3P_2 \rightarrow {}^3P_1$), hereafter CI (1–0) and CI (2–1), respectively). We represent a galaxy by a three-dimensional distribution of molecular clouds (PDRs) at parsec scale resolution and then apply radiative transfer and line-tracing calculations to each molecular cloud to calculate the emitted line radiation of chemical species by the galaxy. (We do not discuss thermal dust continuum properties that dominate the broad-band sub-mm emission of galaxies). We use these models to explore the sub-mm line-properties of galaxies at $z = 2.0$ and $z = 1.2$, how they shape the SF in galaxies, how these compare to similar galaxies in the local Universe, and to make qualitative predictions for future ALMA surveys. We aim to understand, from a theoretical perspective, how the physics that drives the formation of stars in galaxies during the SF peak of the Universe compares to SF in local galaxies and how we can test this. We limit our study to normal star-forming galaxies, representative of average galaxies on the star-forming 'main sequence', rather than focusing on the more extreme starburst galaxies. Galaxies at $z = 2.0$ belong to the population during the peak of SF activity of the Universe. Galaxies at $z = 1.2$ belong to the tail-end of the population responsible for the SF that likely produced the bulk of stars in massive galaxies. Star-forming galaxies at these redshifts are very favourable for ALMA observations, since one can observe multiple CO lines, HCN and (both) carbon fine structure lines at these redshifts with a limited number of bandpasses. The [C II] and high-J CO lines can be observed towards galaxies at redshift $z = 2.0$.

The structure of the paper is as follows. In Section 2 we present the theoretical modelling tools used to obtain our predictions. In Section 3 we present our predictions for the sub-mm line properties of local and high-redshift galaxies and how they correlate with typical galaxy properties. In Section 4 we discuss our findings and we summarize our work in Section 5. Throughout this paper we adopt a flat ΛCDM cosmology with $\Omega_0 = 0.28$, $\Omega_\Lambda = 0.72$, $h = H_0/(100 \, \text{km s}^{-1} \, \text{Mpc}^{-1}) = 0.70$, $\sigma_8 = 0.812$ and a cosmic baryon fraction of $f_b = 0.1658$ (Komatsu et al. 2009).

2 MODEL

Our model to study the sub-mm properties of galaxies consists of three parts. The first part of the machinery is a semi-analytic galaxy formation model (see Section 2.1), which we use to create
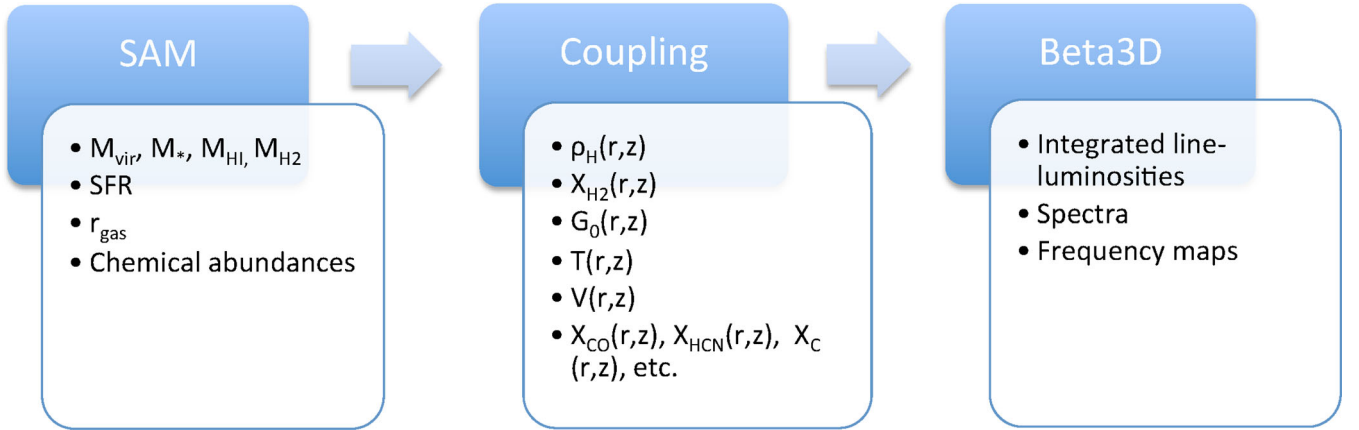
Figure 1. Flowchart of our three-step model to calculate the sub-mm line intensity from atomic and molecular species in galaxies. The blue boxes represent the three individual parts of the model. The white boxes show the relevant output from each individual step which also acts as input for the following step.

Table 1. Summary of the free parameters associated with the three-dimensional radiative-transfer and line tracing code, and its coupling with the galaxy formation model.

Parameter	Description	Value	Reference
L_{grid}	Grid size	180 pc	Section 2.2.1
R_{extent}	Radius out to which disc is integrated	$4.5 \times R_g$	Section 2.2.1
$G_{background}$	Uniform background radiation field	1.6×10^{-3} erg cm^{-2} s^{-1} (Habing Flux)	Section 2.2.3
σ_{gas}	Vertical velocity dispersion of cold gas	10 km s^{-1}	Leroy et al. (2008)

a mock sample of galaxies with global properties such as cold gas mass, H_2 fraction, SFR, and size. The second part is made up of a series of routines to create 3D realizations of the galaxies in the mock sample (see Section 2.2), consisting of key properties such as density distribution, temperature, and velocity field. The final part of the machinery is a three-dimensional radiative-transfer and line tracing code (β3D; see Section 2.3), which provides integrated luminosities, spectra and frequency maps of molecular and atomic lines for our mock sample of galaxies. The overall process, including the output of each step which also acts as input for the following step, is depicted in Fig. 1. We provide a summary of the important free parameters associated with β3D and the coupling between the galaxy formation model and β3D in Table 1. In the following sections we discuss the individual elements of the machinery in detail.

2.1 Galaxy formation model

The backbone of our galaxy formation model to create mock galaxies is the SAM described in Popping et al. (2014) and Somerville et al. (2008b, 2012). The model tracks the hierarchical clustering of dark matter haloes, radiative cooling of gas, SF, SN feedback, AGN feedback (in two distinct modes, quasars and radio jets), galaxy mergers, starbursts, the evolution of stellar populations, and the effects of dust obscuration. We refer the reader to the above-mentioned papers for a detailed description of the model and leave the free parameters associated with the galaxy-formation model fixed at the values discussed in Popping et al. (2014). In the remaining of this section we discuss the physical processes in the model relevant to this work.

When gas cools on to a galaxy, we assume it initially collapses to form a rotationally supported disc. The scale radius of the disc is computed based on the initial angular momentum of the gas and

the halo profile, assuming that angular momentum is conserved and that the self-gravity of the collapsing baryons causes contraction of the matter in the inner part of the halo (Blumenthal et al. 1986; Flores et al. 1993; Mo, Mao & White 1998). Assuming that the halo initially has a density profile described by the Navarro–Frenk–White (NFW; Navarro, Frenk & White 1996) form, the size of the gas disc of a galaxy is given by

$$R_g = \frac{1}{\sqrt{2}} f_j \lambda R_{vir} f_c^{-1/2} f_R(\lambda, c, f_d), \tag{1}$$

where λ is the halo spin parameter (at redshift zero the distribution of λ typically has a mean of ~ 0.035 with a standard deviation of 0.5), $f_j \equiv (J_d/m_d)/(J_h/M_{vir})$ is the ratio of the specific angular momentum of the disc and the halo, c is the NFW concentration of the halo, and f_d is the disc mass to the halo mass ratio. The parameter $f_c^{-1/2}$ corrects for the difference in energy of the NFW profile relative to that of a singular isothermal profile, and f_R accounts for the adiabatic contraction (see Mo et al. 1998, for expressions governing f_R and f_c). Somerville et al. (2008a) showed that this approach produces good agreement with the evolution of the size–stellar mass relation for disc-dominated galaxies from $z \sim 2$ to the present. This approach also reproduces the observed sizes of H I discs in the nearby Universe, the observed sizes of CO discs in local and high-redshift galaxies, and the spatial extent of the SFR density in nearby and high-redshift galaxies (Popping et al. 2014).

We assume that the cold gas consists of an ionized, atomic and molecular component. The H_2 component acts as an important collision partner and may form in dense regions where the gas is self-shielded against impinging radiation. The cold gas is distributed in an exponential disc with radius r_{gas}. We divide the cold gas in radial annuli and compute the fraction of H_2 in each annulus as described below.

We compute the H_2 fraction of the cold gas in an annulus based on the simulation by Gnedin & Kravtsov (2011), who performed high-resolution 'zoom-in' cosmological simulations with the Adaptive Refinement Tree (ART) code of Kravtsov (1999), including gravity, hydrodynamics, non-equilibrium chemistry, and 3D on-the-fly radiative-transfer. Based on their simulations, the authors find a fitting function for the H_2 fraction which effectively parameterizes f_{H2} as a function of dust-to-gas ratio relative to the Milky Way, D_{MW}, the UV ionizing background relative to the Milky Way, U_{MW}, and the neutral gas surface density Σ_{HI+H_2}. The fraction of molecular hydrogen is given by

$$f_{H_2} = \left[1 + \frac{\tilde{\Sigma}}{\Sigma_{HI+H_2}}\right]^{-2} \qquad (2)$$

where

$$\tilde{\Sigma} = 20 \, M_\odot \, pc^{-2} \frac{\Lambda^{4/7}}{D_{MW}} \frac{1}{\sqrt{1 + U_{MW} D_{MW}^2}},$$

$$\Lambda = \ln(1 + g D_{MW}^{3/7} (U_{MW}/15)^{4/7}),$$

$$g = \frac{1 + \alpha s + s^2}{1 + s},$$

$$s = \frac{0.04}{D_* + D_{MW}},$$

$$\alpha = 5 \frac{U_{MW}/2}{1 + (U_{MW}/2)^2},$$

$$D_* = 1.5 \times 10^{-3} \ln(1 + (3U_{MW})^{1.7}).$$

The local UV background relative to the Milky Way is set by relating the SFR of the galaxy in the previous time-step to the Milky Way SFR as $U_{MW} = \frac{SFR}{SFR_{MW}}$, where we choose $SFR_{MW} = 1.0 \, M_\odot \, yr^{-1}$ (Murray & Rahman 2010; Robitaille & Whitney 2010). We take the dust-to-gas ratio to be proportional to the metallicity in solar units $D_{MW} = Z/Z_\odot$.

SF is modelled based on the empirical relationship found by Bigiel et al. (2008) between SFR surface density and H_2 surface density. Observations of high-density environments in starbursts and high-redshift objects indicate that above some critical H_2 column density, the relationship between SFR surface density and H_2 surface density steepens. To account for this steepening, we introduce a two-part process to form stars,

$$\Sigma_{SFR} = A_{SF} \, \Sigma_{H_2} / (10 M_\odot pc^{-2}) \left(1 + \frac{\Sigma_{H_2}}{\Sigma_{H_2,crit}}\right)^{N_{SF}}, \qquad (3)$$

with $A_{SF} = 4.4 \times 10^{-3} \, M_\odot \, yr^{-1} \, kpc^{-2}$, $\Sigma_{H_2,crit} = 100 \, M_\odot \, pc^{-2}$, and $N_{SF} = 0.5$.

We use the approach presented in Arrigoni et al. (2010) to include detailed metal enrichment by Type Ia and Type II SN and long lived stars. The chemical enrichment extension allows the tracking of stellar and gas abundances of individual chemical elements. Although this extension was originally developed with the Somerville et al. (2008b) models as its backbone, we have incorporated this machinery into the newest version of the SAMs used in this paper. We refer the reader to Arrigoni et al. (2010) for a detailed description of the chemical enrichment model.

2.2 Coupling the codes

Although SAMs are suitable for modelling the global properties of galaxies, they lack the spatial information to properly model the contribution of individual molecular clouds to the emitted sub-mm spectra of galaxies. In this subsection we describe our methodology for creating a three-dimensional representation at parsec-level resolution of model galaxies generated using our SAMs. We will discuss the galaxy properties that are needed as input for the 3D radiative-transfer and line tracing code discussed in Section 2.3.

2.2.1 Gas densities

For an exponential disc, the effective central hydrogen gas density seen from any radius r in the disc is defined as

$$n_0(r) = \frac{M_H}{4\pi m_H R_g^2 z_g(r)} \qquad (4)$$

where M_H is the total hydrogen mass (atomic plus molecular) of the galaxy, m_H the mass of a single hydrogen atom, R_g the gas scale length of the galaxy and $z_g(r)$ the gas scale height.

The scale height $z_g(r)$ of the gaseous disc is calculated assuming vertical equilibrium, where the gravitational force is balanced by the pressure of the gas $P(r) = \sigma_{gas}^2 \rho_g(r)$, where $\rho_g = \Sigma_{gas}(r)/2z_g(r)$, and σ_{gas} is the vertical velocity dispersion of the gas in the disc which we assume to be constant, $\sigma_{gas} = 10 \, km \, s^{-1}$ (Leroy et al. 2008). Following Popping et al. (2012) we can express the pressure acting on the disc as

$$P_m(r) = \frac{\pi}{2} G \Sigma_{gas}(r) \left[\Sigma_{gas}(r) + \frac{\bar{f}_\sigma}{4} \sqrt{\Sigma_*(r)\Sigma_*^0}\right], \qquad (5)$$

where $\bar{f}_\sigma = 0.4$, $\Sigma_*(r)$ is the stellar surface density and Σ_*^0 is the central stellar surface density. We can now solve for z_g to find

$$z_g(r) = \frac{\sigma_{gas}^2}{\pi G \left[\Sigma_{gas}(r) + 0.1\sqrt{\Sigma_*(r)\Sigma_*^0}\right]}. \qquad (6)$$

The hydrogen density at any point in the galaxy can now be expressed as

$$n_H(r, z) = n_0(r) \exp\left(-\frac{r}{R_g}\right) \exp\left(-\frac{|z|}{z_g(r)}\right). \qquad (7)$$

This approach is similar to that presented in Berry et al. (2014), although we do not assume the ratio between gas scale height and scale length χ_z to be fixed, but rather calculated the gas scale height at every point in the disc. We adopt a resolution of 180 pc and integrate the discs out to 4.5 times their scale radii.

2.2.2 H_2 abundance

The local H_2 abundance of cold gas is dependent on the local cold gas (column) density, whereas SAMs only provide the global H_2 abundance. We therefore need to recalculate the H_2 abundance in every grid cell. The self-shielding transition of H_2 is rather sharp for an impinging UV-radiation field in a PDR (see equations 36 and 37 of Draine & Bertoldi 1996). We therefore may assume that the cold gas in grid cells with a visual extinction of $A_v > 2.0$ mag is fully molecular (i.e. the fractional abundance $X_{H2} = 0.5$) and for $A_v < 1.0$ mag one has the minimal H_2 abundance as suggested by the SAMs. The visual extinction of a grid cell is defined as $A_v = N_H/2 \times 10^{21} (mag)$, where N_H is the hydrogen column density of the grid cell. We ascribe H_2 abundances to grid cells with $1.0 < A_v < 2.0$ mag by logarithmic interpolation between the abundances set for visual extinction magnitudes $A_v = 1.0$ mag and $A_v = 2.0$ mag.

2.2.3 Impinging radiation field

The radiation field G_{UV} impinging on a giant molecular cloud (GMC) depends on the transmission of UV photons from star-forming regions and their propagation through the diffuse ISM. The exact UV field strength depends on the local conditions in the ISM, such as optical depth and the ratio of gas and dust in the diffuse ISM and in GMCs. We scale G_{UV} as a function of the local SFR in each individual grid cell. The SFR within a grid cell is calculated following equation (3). We can convert the local SFR to a UV radiation field G_{UV} by relating the SFR surface density within a grid cell to the UV radiation-field as

$$\frac{G_{UV}}{G_0} = \left(\frac{\Sigma_{SFR}}{\Sigma_{SFR}^0} \right). \tag{8}$$

We choose $\Sigma_{SFR}^0 = 10^{-3} \, M_\odot \, \mathrm{yr}^{-1} \, \mathrm{kpc}^{-2}$, to assure $G_{UV} = G_0 = 1.6 \times 10^{-3} \, \mathrm{erg \, cm}^{-2} \, \mathrm{s}^{-1}$ (the Habing Flux) for the solar neighbourhood. We also include a uniform local background radiation field of 1 G_0.

2.2.4 Temperature

The temperature within a PDR is set by the balance between heating and cooling processes. Cooling of PDRs occurs predominantly through fine-structure lines of abundant atoms and ions. In the moderately dense ISM ($n < n_{cr} \approx 1 \times 10^4 \, \mathrm{cm}^{-3}$), the cooling is mainly dominated by [C II], whereas the [O I] 63 μm fine-structure line is important in higher density regions. Tielens (2005) shows that in the high-density limit (where [O I] is the dominant coolant) the energy balance of a steady system can be written as

$$\frac{\exp(-y)}{y^{1.17}} = \frac{3.4\gamma}{1 + 2.5\gamma^{0.73}}, \tag{9}$$

where

$$y = \frac{228 \, K}{T} \tag{10}$$

and γ is the ionization parameter defined as $G_0 T^{1/2}/n$ with $n_e = 1.4 \times 10^{-4} n$. γ measures the ionization rate over the recombination rate, the efficiency of the photoelectric effect. These expressions can be solved iteratively for the temperature T for a given density n and impinging radiation field G_{UV}.

In the lower density regime, where [C II] is the dominant coolant, we can solve for the temperature using a similar set of equations,

$$\frac{\exp(-y')}{y'^{1/2}} = \frac{1.7\gamma}{1 + 2.5\gamma^{0.73}} \tag{11}$$

where

$$y' = \frac{92 \, K}{T}. \tag{12}$$

Up to this point we have neglected the contribution to the total cooling through molecules (especially CO). CO acts as a good coolant for cold gas due to its ability to radiate at relatively low temperatures and densities. However, the cooling rate is difficult to calculate because lower-J CO lines are optically thick. A photon emitted by a molecule in the $J = 1$ state is likely to be re-absorbed by another molecule in the $J = 0$ state. This process effectively only moves the energy around within the molecular cloud without contributing to the overall net cooling. Molecules in these low states only contribute to the cooling when they are within approximately one optical depth from the cloud surface, restricting the cooling only to a small fraction of the cloud volume. Emission from high-J

levels of CO is optically thin and can escape the cloud; however, the temperatures and densities required to excite these molecules up to high-J levels are generally high ($\sim 10^5 \, \mathrm{cm}^{-3}$ and ~ 100 K). In the environments typical of normal star-forming galaxies, there are therefore only a few molecules in these high states, which strongly suppresses cooling from these molecules.

2.2.5 Velocity field

In addition to the density and temperature of the cold gas, the 3D radiative-transfer simulation requires the velocity field of the gas as one of its initial conditions for the line-tracing. Furthermore it allows the creation of frequency or velocity maps of sub-mm emission when a velocity field of the disc is provided (Pérez-Beaupuits et al. 2011). We derive the velocity field following the approach presented in Obreschkow et al. (2009). We refer the reader to that work for a detailed description of the methodology, but present the main ingredients of their approach. The circular velocity profile of gas in a disc comprises three components, the halo, the galaxy disc and the bulge of the galaxy,

$$V_c^2(x) = V_{c,\mathrm{halo}}^2(x) + V_{c,\mathrm{disc}}^2(x) + V_{c,\mathrm{bulge}}^2(x), \tag{13}$$

where $x = r/r_{vir}$, and r_{vir} is the virial radius of the halo. Each galaxy is situated in a dark matter halo with an NFW profile. The concentration parameter of the halo c_{halo} and its virial radius r_{vir} are both provided by the galaxy formation model. Assuming a spherical halo, the circular velocity of the gas contributed by the halo mass is given by

$$V_{c,\mathrm{halo}}^2(x) = \frac{G \, M_{vir}}{r_{vir}} \times \frac{\ln(1 + c_{halo}x) - \frac{c_{halo}x}{1 + c_{halo}x}}{x \left[\ln(1 + c_{halo}x) - \frac{c_{halo}}{1 + c_{halo}} \right]}, \tag{14}$$

where M_{vir} is the virial mass of the halo.

Under the assumption that the radial density distribution of a galaxy disc can be described by an exponential, Obreschkow et al. (2009) find that the circular velocity of cold gas due to the disc can be approximated by

$$V_{c,\mathrm{disc}}^2(x) \approx \frac{GM_{disc}}{r_{vir}}$$
$$\times \frac{c_{disc} + 4.8c_{disc} \exp[-0.35c_{disc}x - 3.5/(c_{disc}x)]}{c_{disc}x + (c_{disc}x)^{-2} + 2(c_{disc})^{-1/2}}, \tag{15}$$

where $c_{disc} = r_{vir}/r_{disc}$ and M_{disc} the sum of the stellar and gaseous component of the disc.

Following Obreschkow et al. (2009), we assume that the bulges of all galaxies are spherical, and that their density profiles can be described by a Plummer potential (Plummer 1911), with a characteristic radius $r_{Plummer} \approx 1.7 \, r_{bulge}$ and $r_{bulge} \approx 0.05 \, r_{disc}$. The circular velocity profile component due to the bulge is

$$V_{c,\mathrm{bulge}}^2(x) = \frac{GM_{bulge}}{r_{vir}} \times \frac{(c_{bulge}x)^2 c_{bulge}}{[1 + (c_{bulge}x)^2]^{3/2}}, \tag{16}$$

where $c_{bulge} = r_{vir}/r_{Plummer}$ and M_{bulge} is the mass of the bulge.

With an expression for the circular velocity profiles of the halo, disc, and bulge, we can now calculate the circular velocity of the cold gas at any location in the disc. The vertical velocity dispersion of the cold gas σ_{gas} is responsible for the motions of the gas perpendicular to the disc. Observations in the local Universe have shown that the vertical velocity dispersion of the cold gas $\sigma_{gas} \approx 10 \, \mathrm{km \, s}^{-1}$ and is approximately constant over the disc (e.g. Shostak & van der Kruit

1984; Leroy et al. 2008). We ascribe a vertical velocity to each grid cell by randomly picking a velocity from a Gaussian distribution centred around $0 \, \text{km s}^{-1}$ with a standard deviation of $10 \, \text{km s}^{-1}$. We estimate the local turbulent velocity dispersion within a GMC following Larson (1981), evaluated for the physical size of a grid cell in the model.

2.2.6 Abundances

Good estimates of the abundances of the various species are fundamental to properly model the line contribution from atomic and molecular species. We already discussed the H_2 abundance of the cold gas in detail in Section 2.2.2; however, we also need to take into account the atoms, molecules and ions of interest to us.

The latest version of our SAMs includes detailed tracking of the abundance of single elements in the cold gas (Arrigoni et al. 2010). We use this model to calculate the carbon and oxygen abundance of the ISM.

The CO abundance of the cold gas is calculated as the amount of carbon locked up in CO. The fraction of the carbon mass locked up in CO has an explicit dependence on metallicity. Following Wolfire, Hollenbach & McKee (2010) we calculate this fraction as

$$f_{CO} = f_{H2} \times \exp\left[-4\left(0.52 - 0.045 \ln\frac{G_{UV}/G_0}{n_H} \right. \right.$$
$$\left. \left. - 0.097 \ln Z' \right) \middle/ A_v \right], \tag{17}$$

where Z' is the metallicity of the cold gas expressed in solar units.

We adopt an HCN abundance of 10^{-8} with respect to the molecular gas, and scale the C^+ abundance with the abundance of carbon in the cold gas. These choices yield good agreement with predictions from Meijerink & Spaans (2005) for the typical range of densities and radiation fields relevant to our work.

2.3 3D radiative-transfer and line-tracing code

We use the advanced fully three-dimensional radiative-transfer code β3D (Poelman & Spaans 2005, 2006) optimized for heavy memory usage by Pérez-Beaupuits et al. (2011). The optimized version was initially developed to calculate the three-dimensional transfer of line radiation in $256 \times 256 \times 128$ element data cubes at a spatial resolution of 0.25 pc, but works as well for different shaped data cubes at different resolutions.

The code requires density, H_2 abundance, temperature, impinging radiation field, and velocity as ambient conditions in each grid cell to calculate the transfer of line radiation of molecules by use of a non-local escape probability formalism. We refer the reader to Poelman & Spaans (2005) for a detailed description of the radiative-transfer method.

Level populations of different atomic and molecular species (in this study C^+,C,O, ^{12}CO and HCN) are calculated using collision rates available in the LAMDA data base (Schöier et al. 2005). We use H_2 as the main collision partner for the radiative transfer calculations of all the molecules and also include the contribution of helium atoms to the total collision density for CO and HCN (following Pérez-Beaupuits et al. 2011). We include the contribution from atomic hydrogen and electrons for the collision rates of C, O, and C^+. The densities of the collisional partners are derived from the galaxy formation model.

The intensity from molecules is dependent on the distribution of level populations, which depends on the temperature and the density of the gas (through collisions with other molecules and atoms as well as a background impinging radiation field). There are large differences in the collisional densities necessary to excite different energy levels. For example, the density needed to populate the $J = 1$ state of CO through collisional excitation is $\sim 10^2$–$10^3 \, \text{cm}^{-3}$, whereas it is already $\sim 10^4 \, \text{cm}^{-3}$ for the $J = 3$ state. These densities arise in different regions of the GMCs, the former being the diffuse GMC atmospheres and the latter the dense GMC core. Densities used in the radiative-transfer calculations in this work were calculated by post-processing the results from the galaxy formation model, smoothed to a resolution of 180 pc (see Sections 2.1 and 2.2). At this resolution, the smoothed density profile of our galaxy never exceeds densities of a few times $10^3 \, \text{cm}^{-3}$, typical for the diffuse outer parts of the GMC, and a sub-grid approach is necessary to account for radiation from denser environments.

Numerical simulations often describe the structure of the ISM with a lognormal (LN) probability distribution function (PDF) (e.g. Wada & Norman 1999, 2007; Krumholz & McKee 2005; Hennebelle & Chabrier 2008, 2009; Price, Federrath & Brunt 2011):

$$f(\rho)d\rho = \frac{1}{\sqrt{2\pi}\sigma} \exp\left[-\frac{\ln(\rho/\rho_0)^2}{2\sigma^2} \right] d\ln\rho, \tag{18}$$

where ρ_0 is the characteristic density and σ the dispersion of the distribution. Numerical simulations suggest that σ can be expressed in terms of the one-dimensional Mach number of turbulence M (e.g. Ostriker, Stone & Gammie 2001; Lemaster & Stone 2008; Price et al. 2011):

$$\sigma^2 \approx \ln(1 + 3M^2/4). \tag{19}$$

The Mach number is calculated as the ratio between the local turbulent velocity (Δv_d) and the sound speed (c_s) of the medium. The local turbulent velocity is estimated following Larson (1981), evaluated for the physical size of a grid cell in the model. The volume-averaged density of a LN distribution is given by

$$\langle\rho\rangle_V = \rho_0 e^{2\sigma^2}. \tag{20}$$

In our case the volume-averaged density of each grid-cell is also given by equation (7). We can therefore express the characteristic density ρ_0 as

$$\rho_0 = \frac{\langle\rho\rangle_V}{e^{2\sigma^2}}. \tag{21}$$

We assume that a grid-cell is made up by small molecular clouds drawn from the LN-PDF. We calculate the contribution of each of the individual molecular clouds within the sub-grid to the emitted radiation, taking the overlap in optical depth space of the molecular clouds into account.

Line intensities are computed using a ray-tracing approach, including the effects of kinematic structures in the gas and optical depth effects. The emerging specific intensity is computed using the escape probability formalism presented in Poelman & Spaans (2005),

$$dI_\nu^z = \frac{1}{4\pi} n_i A_{ij} h\nu_{ij} \beta(\tau_{ij}) \left(\frac{S_{ij} - I_b^{loc}(\nu_{ij})}{S_{ij}} \right) \phi(\nu)dz, \tag{22}$$

where dI_ν^z has units of $\text{erg cm}^{-2} \, \text{s}^{-1} \, \text{sr}^{-1} \, \text{Hz}^{-1}$, n_i is the population density in the ith level, A_{ij} the Einstein A coefficient, $h\nu_{ij}$ the energy difference between the levels i and j, β the escape probability of a photon, τ_{ij} the cumulative optical depth, and $\phi(\nu)$ the Doppler correction to the photon frequency due to local turbulence inside the cloud and large-scale bulk motions. S_{ij} is the source function of
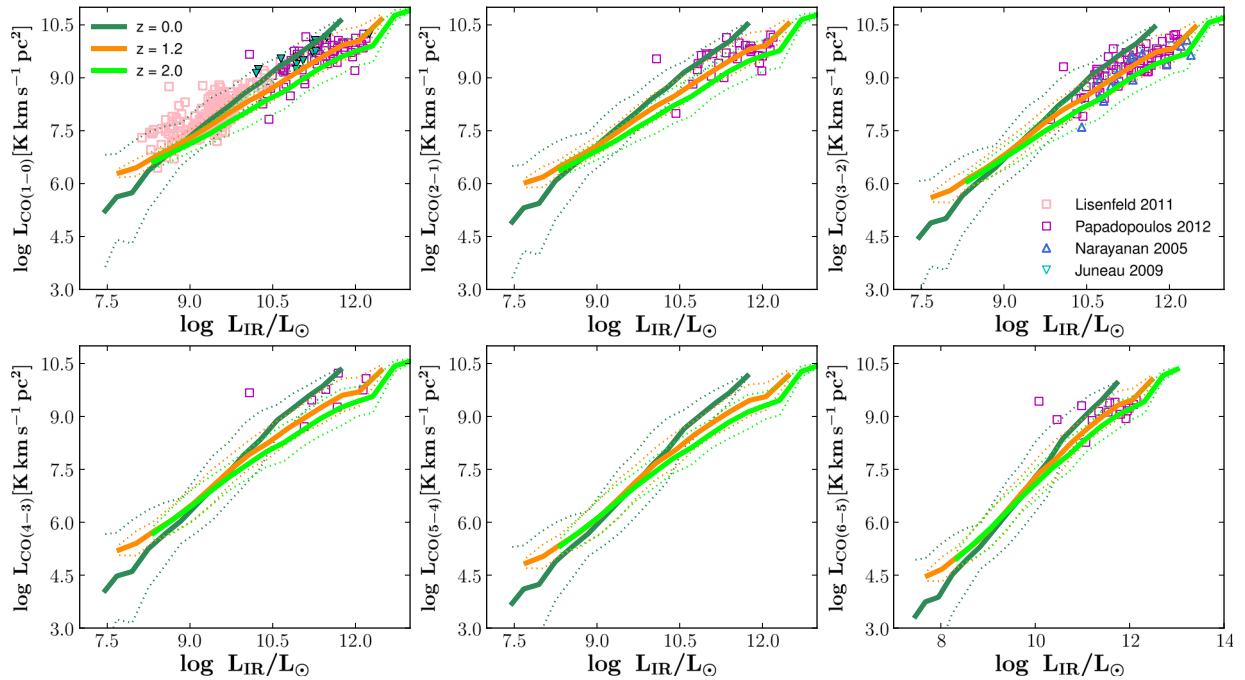
Figure 2. CO line-luminosity of CO $J = 1 - 0$ up to CO $J = 6 - 5$ as a function of FIR luminosity. Model results are compared to observations taken from Narayanan et al. (2005), Juneau et al. (2009), Lisenfeld et al. (2011), and Papadopoulos et al. (2012). The solid lines show the median of the model predictions, whereas the dotted lines represent the two sigma deviation from the median.

the corresponding medium, and $I_{\rm b}^{loc}(\nu_{ij})$ the local continuum background radiation at the field frequency ν_{ij}. The local background $I_{\rm b}^{loc}(\nu_{ij})$ is caused by the local dust emission (calculated following Hollenbach, Takahashi & Tielens 1991) and is slowly varying with frequency.[1] The code uses a multi-zone radiative-transfer approach in which the emerging specific intensity is dependent on the different escape probabilities within a grid-cell as well as connecting adjacent grid points along the line of sight. This makes our approach more physical compared to the purely local nature of the LVG approximation.

3 RESULTS

In this section we present the predictions of our model for different atomic and molecular species. The simulations were run on a grid of haloes with virial masses ranging from $1 \times 10^9 \, \rm M_\odot$ to $5 \times 10^{14} \, \rm M_\odot$, with a mass resolution of $1 \times 10^7 \, \rm M_\odot$. Throughout the rest of the paper, we only consider central galaxies with a bulge-to-total mass ratio of 0.4 and smaller, and gas fractions of $f_{\rm gas} > 0.1$. We first discuss the predicted CO line emission from model galaxies and how line ratios can potentially be used to constrain the gas physics in play in galaxies. We will continue with similar discussions for HCN, atomic and ionized carbon, and oxygen, after which we will discuss the cooling properties of the modelled galaxies.

3.1 CO

Because of its relatively high abundance ($\sim 10^{-4}$), the emission of CO is commonly used as a tracer of the ISM. Indeed, in the last decade surveys have probed the CO emission of local galaxies with

---

[1] We note that this is an extension to the model presented in Pérez-Beaupuits et al. (2011).

a broad range of properties (e.g. Helfer et al. 2003; Narayanan et al. 2005; Leroy et al. 2008; Lisenfeld et al. 2011; Papadopoulos et al. 2012; Bauermeister et al. 2013), adding a great wealth of information about the molecular content of local galaxies. In Fig. 2 we present our predictions for CO line luminosities up to CO $J = 6 - 5$ as a function of FIR luminosity in local galaxies. Observations were taken from Narayanan et al. (2005), Juneau et al. (2009), Lisenfeld et al. (2011), and Papadopoulos et al. (2012). We find that the CO luminosity of galaxies increases monotonically with increasing FIR luminosity for all CO transitions. We find a good match between model predictions and observations over a wide range of FIR luminosities for the CO $J = 1 - 0$ transition, as well as for the higher CO transitions. This is encouraging, as it implies that we do not only correctly reproduce the CO $J = 1 - 0$ emission arising from low-temperature and low-density regions (a few times $10^3 \, \rm cm^{-3}$), but also the CO $J = 6 - 5$ emission from much warmer and denser regions (up to $10^5 \, \rm cm^{-3}$). The CO line luminosity of galaxies at fixed FIR luminosity decreases with increasing redshift. We find a shallower slope in the relation between CO line luminosity and FIR luminosity for galaxies at $z = 1.2$ and $z = 2.0$ than for local galaxies.

Fig. 3 is similar to the previous figure, but shows the emitted CO luminosity as a function of SFR. Observations were taken from Leroy et al. (2008), Daddi et al. (2010), Tacconi et al. (2010, 2013). Similar to the previous figure, the CO luminosity increases monotonically with increasing SFR. We find good agreement with direct observations, both in the local Universe and at high redshift. Again, we note that the critical density and excitation energy of CO $J = 3 - 2$ and CO $J = 2 - 1$ differ by approximately a factor of 2, demonstrating that our model correctly describes the gas physics in play over a range of densities and temperatures.

It is clear from the previous figure (and many of the subsequent figures) that at fixed FIR luminosity modelled galaxies at $z = 1.2$ and $z = 2.0$ emit somewhat less radiation through lines tracing
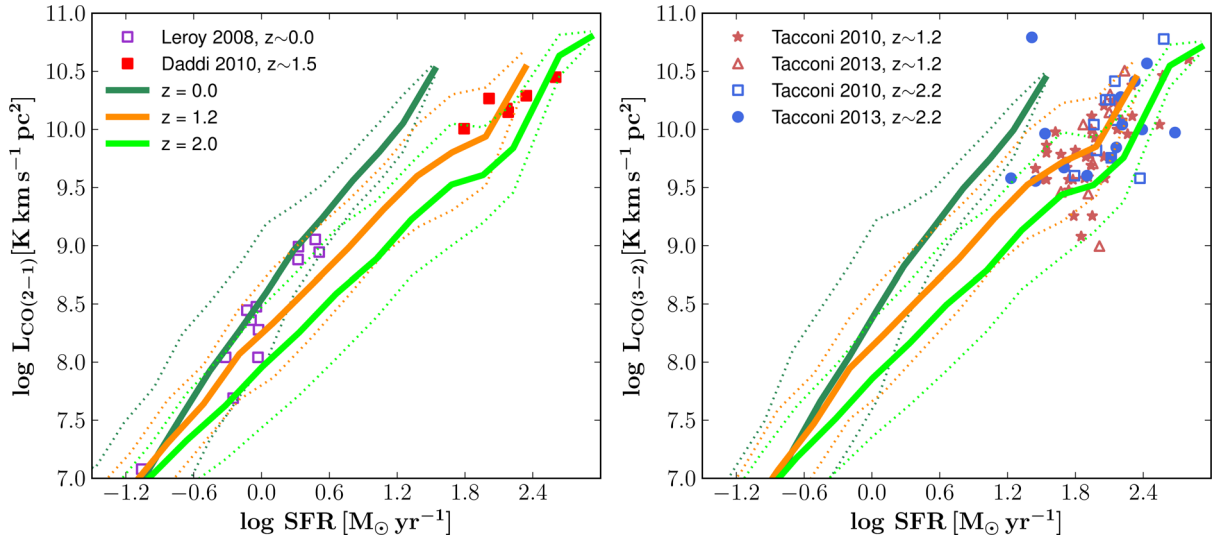
Figure 3. CO-line luminosity of CO $J = 2 - 1$ (left panel) and CO $J = 3 - 2$ (right panel) as a function of SFR for modelled galaxies at $z = 0.0$, $z = 1.2$, and $z = 2.0$. Observations are taken from Leroy et al. (2008), Daddi et al. (2010), Tacconi et al. (2010, 2013).
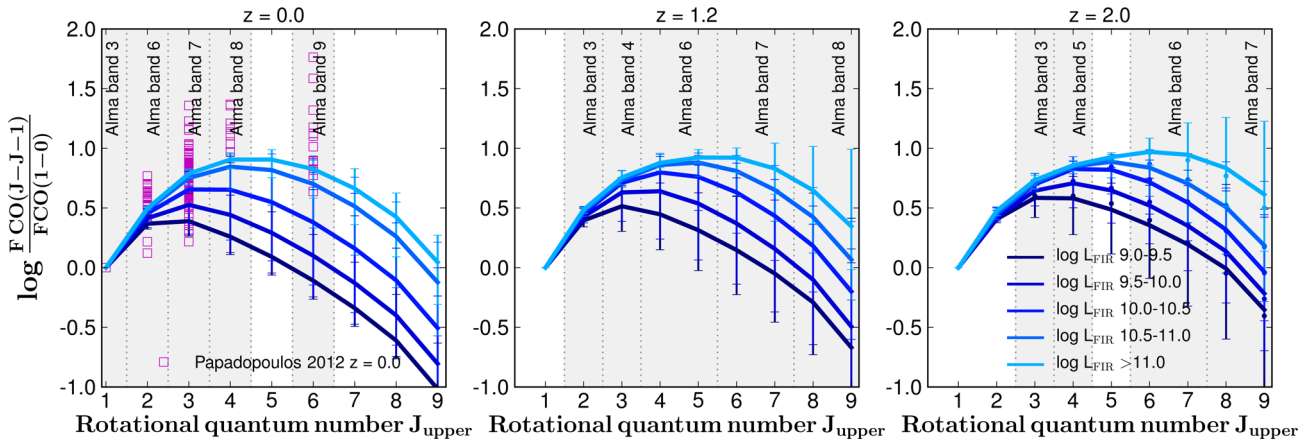

Figure 4. CO SLED of our modelled galaxies at $z = 0.0$ (left panel), $z = 1.2$ (middle panel), and $z = 2.0$ (right panel) separated into bins of FIR luminosity. The SLED is normalized to the CO $J = 1 - 0$ line luminosity. Observations are taken from Papadopoulos et al. (2012). Note the change in CO SLED shape between galaxies at $z = 0.0$, $z = 1.2$, and $z = 2.0$

diffuse and low-density environments. We discuss this in Section 4. The sparse amount of data for typical SF galaxies at high redshift unfortunately does not allow us to further constrain our model predictions, both due to a lack of galaxies with lower SFR and a lack of observations covering a wide enough range of CO lines. We anticipate that in the near future ALMA and other sub-mm telescopes will add significantly to the number of high-redshift galaxies with (multiple) observed CO line-transitions.

The CO Spectral Line Energy Distribution (SLED) of galaxies provides straightforward information about the density and temperature of the dominant SF cold gas. Different densities and temperatures result in a change of peak location in the CO SLED: high CO excitation is achieved through a combination of high kinetic temperature and high density. In Fig. 4 we present the CO SLEDs for our modelled galaxies, compared to observations of CO line ratios by Papadopoulos et al. (2012). The CO SLED is normalized to the CO $J = 1 - 0$ emission. On average our predictions at $z = 0.0$ are in good agreement with the observations. We do not reproduce the highest excitation CO SLEDs from the observational sample. Papadopoulos et al. argue that supersonic turbulence

and high cosmic ray energy densities are necessary to power the extraordinary CO line excitation of these galaxies. We have not included these physical processes in our model. We find that the more FIR-luminous objects peak at higher CO excitations, corresponding to higher kinetic temperatures and densities. This implies that the physical properties of the ISM in the more FIR-luminous objects differ significantly from the ISM in less FIR-luminous objects and that the ISM is not just made up by a larger number of clouds with similar density and temperature.

We see the same trends at high redshifts, where again the FIR-luminous objects have a higher CO-excitation peak. Furthermore, there is a strong difference in shape when comparing the $z = 0.0$, $z = 1.2$, and $z = 2.0$ CO SLEDs at fixed FIR luminosity. For example, galaxies with FIR luminosities $9.5 < \log(L_{FIR}/L_\odot) < 10.0$ show a peak in their CO SLED at the third rotational level, whereas the CO SLED peaks at the fourth rotational level for similar galaxies at $z = 1.2$ and $z = 2.0$, respectively. Analogously, galaxies with FIR luminosities $10.5 < \log(L_{FIR}/L_\odot) < 11.0$ peak at the fourth level in $z = 0.0$ galaxies, whereas they peak at the fifth level in $z = 1.2$ and $z = 2.0$ galaxies, respectively. There is an even stronger
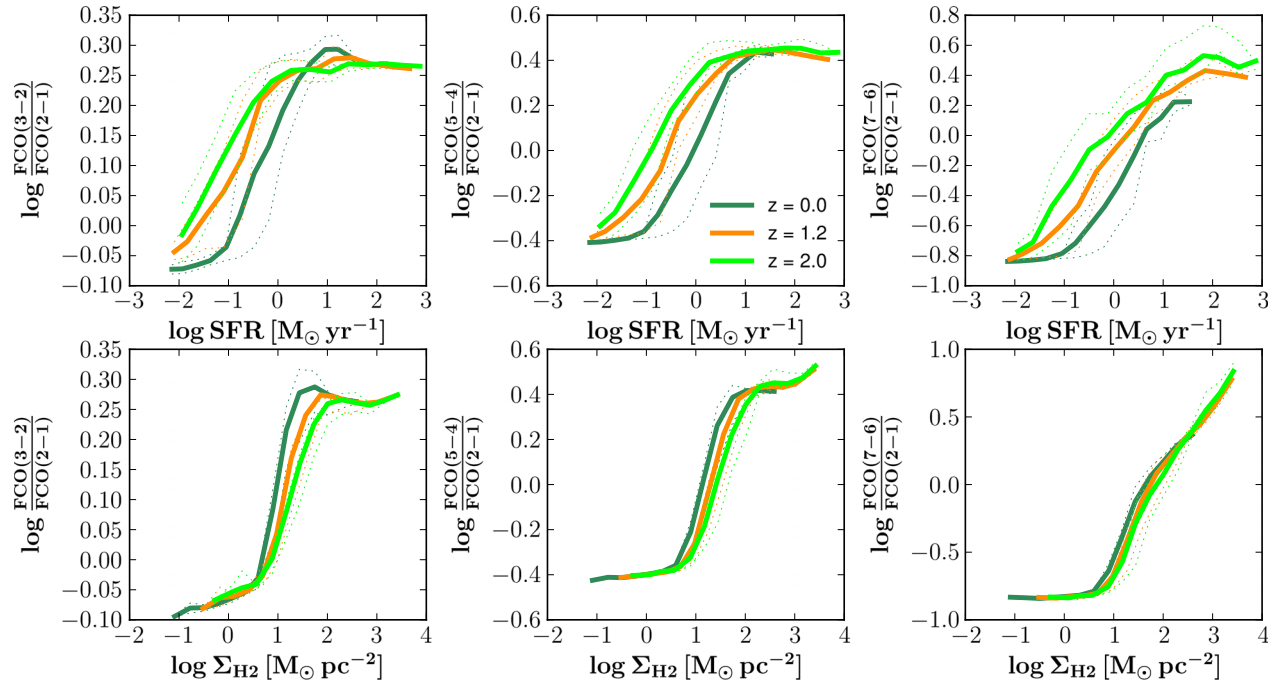
Figure 5. CO line ratios as a function of global galaxy properties at $z = 0.0$, $z = 1.2$, and $z = 2.0$. CO line ratios of interest are CO $J = 3 - 2$/CO $J = 2 - 1$ (left column), CO $J = 5 - 4$/CO $J = 2 - 1$ (middle column), and CO $J = 7 - 6$/CO $J = 2 - 1$ (right column). CO line ratios are plotted as a function of SFR (top row) and cold gas surface density (Σ_{HI+H2}; bottom row). Note the offset in line ratios between galaxies at $z = 0.0$ and higher redshift for the SFR, but the tight correlation in line ratios as a function of cold gas surface density.

evolution in the CO SLED for the most FIR-luminous galaxies $\log (L_{FIR}/L_{\odot}) > 11$. The increment in the excitation peak with redshift is indicative of higher densities and kinetic temperatures. Furthermore, the relative contribution of high excitation CO lines is much larger in the high-redshift modelled galaxies. This strongly favours a scenario in which the ISM in galaxies with fixed FIR luminosities at high redshift is denser and warmer than in their local counterparts. Galaxies at $z = 2.0$ consist of denser and warmer gas than their counterparts at $z = 1.2$.

For a fixed density and temperature a change in CO abundance can affect the shape of the CO SLED. The CO SLED of a molecular cloud peaks at higher rotational levels with increasing CO abundance. To first order the CO abundance of the molecular gas in our galaxies follows the cold gas metallicity, which at fixed FIR luminosity increases with time. If the excitation conditions (gas density and temperature) of galaxies at high redshift would be similar to local galaxies, we would expect the peak in the CO SLED of high-redshift galaxies to move to lower rotational levels due to lower CO abundances. This is in sharp contrast with our predictions, emphasizing that the change in CO SLED with redshift is driven by different excitation conditions.

In Fig. 5 we explore the line ratios of CO transitions as a function of two global galaxy properties. We compare our predicted line ratios with SFR and H_2 surface density. We find a strong increase in CO line ratios as a function of SFR. Most notable is that the increase is more significant when using line ratios tracing larger differences in density and temperature. Whereas we only observe an increase of approximately 0.5 dex in the CO($J = 3 - 2$)/CO($J = 2 - 1$) line ratio, we find an increase of a full dex in the CO($J = 5 - 4$)/CO ($J = 2 - 1$) ratio, and two dex in the CO($J = 7 - 6$)/CO($J = 2 - 1$) ratio. This indicates that with increasing SFR the cold gas contains a much larger fraction of gas clouds with densities of the order of $\sim 10^5$ cm^{-3}. Galaxies at $z = 1.2$ and $z = 2.0$ have

higher CO line ratios than their counterparts with similar SFR at $z = 0$. This is most prominent for galaxies with SFR $< 10 \, M_{\odot}$ yr^{-1}. The difference between the local and high-redshift galaxies also increases when using line ratios tracing larger differences in density and temperature.

The evolution in CO line ratios with H_2 surface density is similar to that with SFR: line ratios increase with increasing FIR luminosity, and the differences become more prominent for line ratios tracing higher densities. The offset in line ratios between high redshift and local galaxies, on the other hand, is negligible. This suggests that CO line ratios are indeed reliable tracers of the density of the dominant gas population of a galaxy, independent of redshift.

3.1.1 CO-to-H_2 conversion

The most common way to estimate the molecular gas mass of a galaxy is through the conversion factor between CO $J = 1 - 0$ luminosity and H_2 mass,

$$\alpha_{CO} = \frac{M_{H2}}{L_{CO}}. \tag{23}$$

Although the CO-to-H_2 conversion appears to be constant in our own Milky Way, there is substantial evidence that this conversion departs from the standard Milky Way value in low-metallicity and high surface density environments (e.g. Schruba et al. 2011; Genzel et al. 2012). Indeed, several efforts have been carried out to model α_{CO} as a function of the metallicity and H_2 surface density of galaxies (Feldmann et al. 2012; Narayanan et al. 2012). We do not aim to provide yet another scaling relation between α_{CO} and galaxy properties, merely to complement previous work.

We present α_{CO} of our modelled galaxies as a function of cold gas metallicity in Fig. 6. The predicted range in α_{CO} is in good agreement with observations of the CO-to-H_2 conversion factor
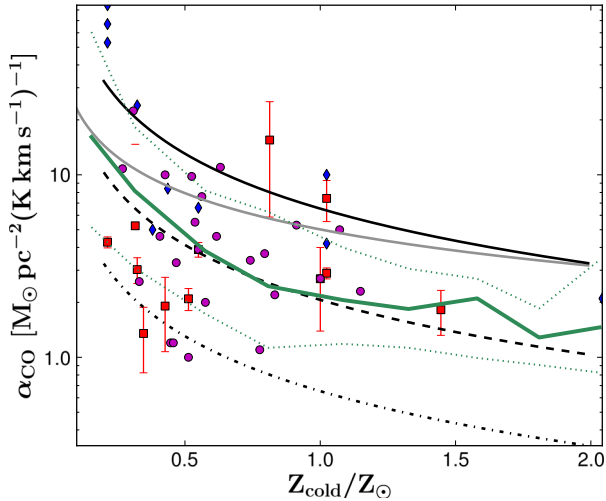
Figure 6. The CO-to-H$_2$ conversion factor α_{CO} in galaxies at $z = 0.0$ as a function of cold gas metallicity (green solid line). The dotted lines mark the 2σ deviation from the mean. Observational measures of α_{CO} were taken from Bolatto et al. (2008, red squares), Leroy et al. (2011, blue diamonds), and Sandstrom et al. (2013, purple circles). Theoretical predictions were taken from Feldmann, Gnedin & Kravtsov (2012, grey solid line) and Narayanan et al. (2012) for an H$_2$ surface density of 10 (black solid), 100 (black dashed) and 1000 (black dash–dotted) M$_\odot$ pc^{-2}.

(Bolatto et al. 2008; Leroy et al. 2011; Sandstrom et al. 2013). We find good agreement with the predictions from the models of Narayanan et al. (2012), but underpredict α_{CO} compared to the results of Feldmann et al. (2012). Our results suggest that there is indeed a variation in the conversion between H$_2$ mass and CO luminosity: α_{CO} rapidly decreases with metallicity at $Z/Z_\odot < 0.5$, driven by low CO abundances. The variation of α_{CO} with metallicity is roughly flat for more metal-rich galaxies. This is in agreement with earlier theoretical work (Feldmann et al. 2012; Narayanan et al. 2012) and observations (Leroy et al. 2011).
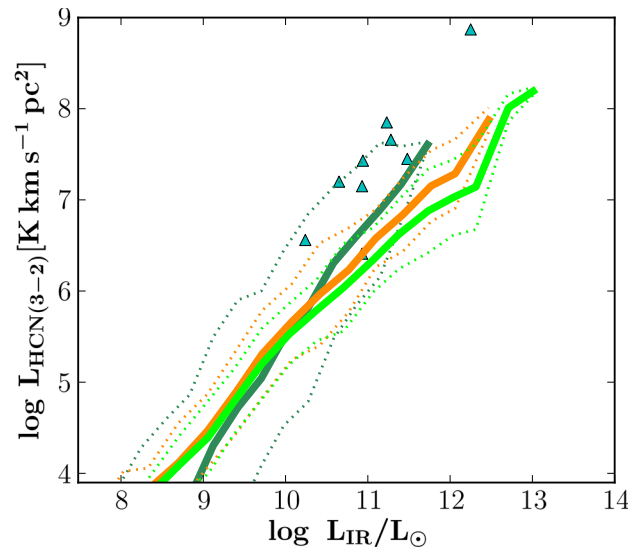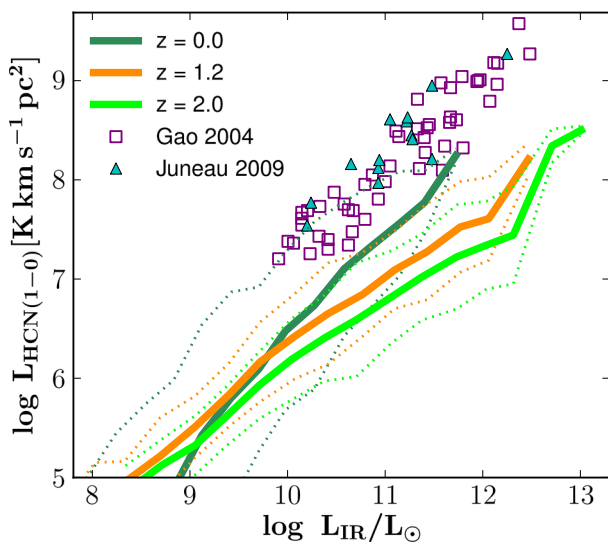
3.2 HCN

High-density star-forming regions are typically observed through emission from HCN (e.g. Loenen et al. 2008). It is one of the most abundant high-dipole-moment molecules that traces gas at densities of the order of 10^5–10^6 cm^{-3}, several orders of magnitudes larger than the low-excitation CO lines. HCN emission is thought to be associated with star-forming GMC cores. Gao & Solomon (2004) found a tight linear correlation between the FIR and HCN luminosity of galaxies, which supports the scenario of HCN being linked to GMC cores.

We find that the HCN $J = 1 - 0$ luminosity of galaxies increases monotonically with FIR luminosity (see Fig. 7, left panel). Assuming that the dust producing the FIR radiation is heated primarily by young massive stars, the FIR luminosity should be proportional to the instantaneous SFR, while the global SFR of a galaxy is linearly proportional to the mass of dense molecular gas. Our predictions for the HCN $J = 1 - 0$ luminosity of galaxies at $z = 0.0$ are slightly too low compared to observations. The HCN $J = 1 - 0$ luminosity in galaxies at redshift $z = 1.2$ and $z = 2.0$ also follows a monotonically increasing trend with FIR luminosity, although there is a minor offset to lower HCN luminosities with respect to our predictions for local galaxies. Unfortunately, the HCN luminosity of high-redshift galaxies is not well constrained by observations. However, our findings are in good agreement with the upper limits presented in Gao et al. (2007). HCN $J = 3 - 2$ traces the densest regions of cold gas ($n \sim 10^7$ cm^{-3}). Similar to HCN $J = 1 - 0$ our model slightly underpredicts the HCN $J = 3 - 2$ luminosity of local galaxies.

The HCN/CO ratio of a galaxy is typically considered as a measure of the very dense (few times 10^5 cm^{-3} to 10^6 cm^{-3}) versus less dense (few times 10^3 to 10^4 cm^{-3}) gas content of a galaxy. In Fig. 8 we plot the HCN $J = 1 - 0$ luminosity of a galaxy versus its CO $J = 1 - 0$ luminosity. We underpredict the HCN $J = 1 - 0$ luminosity of galaxies as a function of their CO $J = 1 - 0$ luminosity compared with observations by Gao & Solomon (2004) and Juneau et al. (2009) by approximately 0.1–0.2 dex. This suggests that our modelled galaxies at $z = 0.0$ have a slightly too-low fraction of very dense cold gas. We find no significant difference
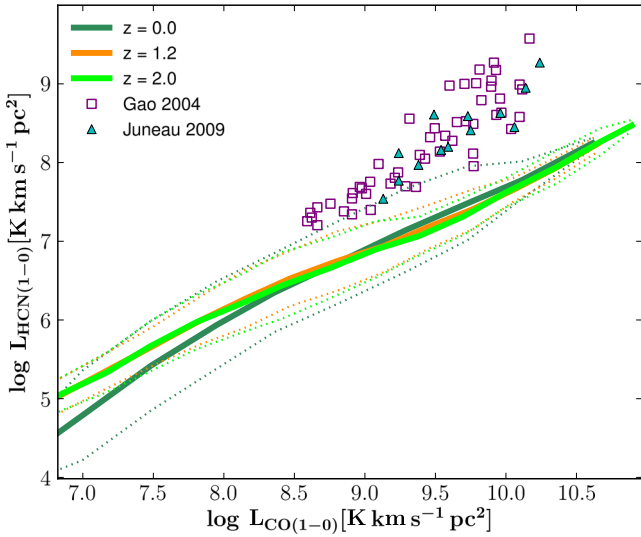

Figure 7. The HCN $J = 1 - 0$ (left panel) and HCN $J = 3 - 2$ (right panel) luminosity of galaxies as a function of its FIR luminosity for galaxies at $z = 0.0$, $z = 1.2$, and $z = 2.0$. Observations of local galaxies are taken from Gao & Solomon (2004) and Juneau et al. (2009).

Figure 8. The HCN $J = 1 - 0$ luminosity of galaxies as a function of its CO $J = 1 - 0$ luminosity at $z = 0.0, z = 1.2$, and $z = 2.0$. Observations are taken from Gao & Solomon (2004) and Juneau et al. (2009).

between the galaxies at $z = 2.0$ and $z = 1.2$ and our predictions for local galaxies.

3.3 Neutral carbon

Because atomic carbon fine-structure emission proceeds through a simple three-level system, detection of the two atomic carbon lines [C I] (1–0) and [C I] (2–1) enables one to derive the excitation temperature and neutral carbon mass of a galaxy independently of other information. This is a powerful tool to study the properties of the atomic gas in galaxies and to break some of the degeneracies frequently found in CO studies (Walter et al. 2011; Carilli & Walter 2013).

We show the relation between FIR luminosity and [C I] (1–0) luminosity in Fig. 9, compared with observations taken from Gerin &
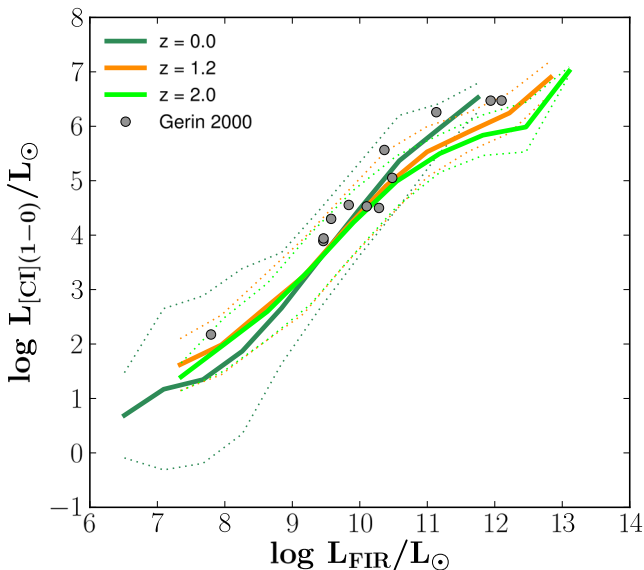

Figure 9. [C I] (1–0) luminosity of modelled galaxies as a function of their FIR luminosity at redshifts $z = 0.0$, $z = 1.2$, and $z = 2.0$. Observations are from Gerin & Phillips (2000).
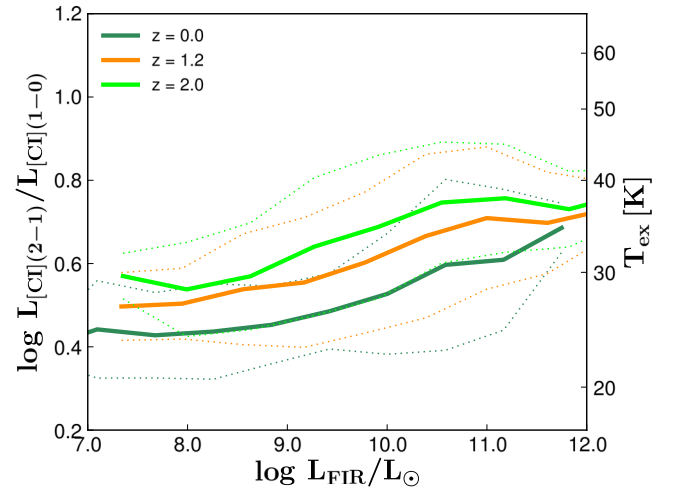

Figure 10. The ratio between [C I] (2–1) and [C I] (1–0) (left axis) or carbon excitation temperature (right axis) as a function of FIR luminosity for modelled galaxies at $z = 0.0$, $z = 1.2$, and $z = 2.0$.

Phillips (2000). The [C I] (1–0) luminosity increases monotonically with FIR luminosity, in good agreement with observations over the entire FIR luminosity range probed. Similar to CO and HCN, we find that high-redshift galaxies have lower [C I] (1–0) luminosities than their local counterparts (at $L_{\rm FIR} > 10^{10} L_{\odot}$). This is driven by an increased SFE, which effectively allows fewer carbon atoms to emit radiation (see Section 4).

In local thermodynamic equilibrium the excitation temperature of carbon can be derived via the formula

$$T_{\rm ex} = 38.8 \times \ln\left(\frac{2.11}{R}\right)^{-1}, \tag{24}$$

where $R = L_{\rm CI(2-1)}/L_{\rm CI(1-0)}$. We present the ratio R and the excitation temperature of carbon of our modelled galaxies in Fig. 10. We find an increase in excitation temperature at $z = 0.0$ for galaxies with FIR luminosities brighter than $L_{\rm FIR} > 10^9 L_{\odot}$. Below this luminosity galaxies have excitation temperatures of roughly 25 K, after which they increase to approximately 35 K for the brightest FIR objects. These excitation temperatures are in good agreement with temperatures found in local galaxies ranging from 20 K in our Galaxy to 50 K in starburst environments (Stutzki et al. 1997; Fixsen, Bennett & Mather 1999; Bayet et al. 2004). Modelled galaxies at high redshift are on average approximately 10–5 K warmer than their local counterparts, and show a similar increase in their temperature with FIR luminosity. The difference in excitation temperature between galaxies at $z = 1.2$ and $z = 2.0$ is negligible.

The ratio between [C I] (1–0) and CO $J = 1 - 0$ is often used to demonstrate that atomic carbon can act as a good tracer of molecular gas in external galaxies (Gerin & Phillips 2000). We find that this ratio is roughly constant in our modelled galaxies at $z = 0.0$ and high redshift with [C I] (1–0)/CO $J = 1 - 0$ =0.08. This is in reasonable agreement with observed ratios in the Milky Way (Fixsen et al. 1999; Ojha et al. 2001; Oka et al. 2005), the local Universe (Israel & Baas 2001, 2002, 2003; Bayet et al. 2004; Israel, Tilanus & Baas 2006) and at high redshift (Weiß et al. 2005; Walter et al. 2011). Indeed, our models suggest that carbon can act as a good tracer of the molecular mass of a galaxy.
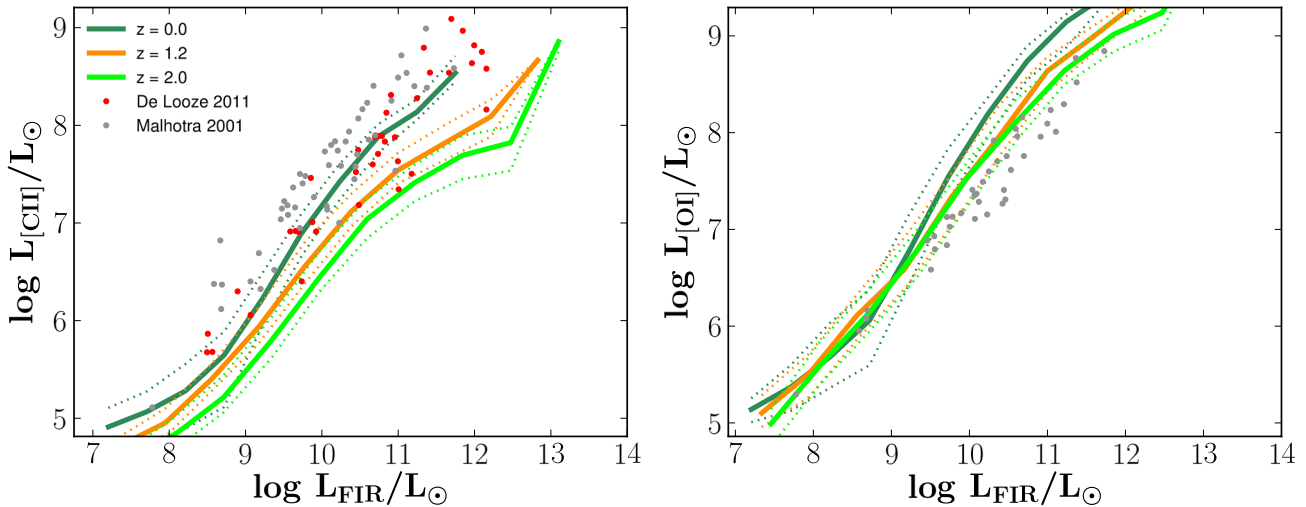
Figure 11. Luminosity of the atomic cooling lines [C II] (158 μm) and [O I] (63 μm) as a function of their FIR luminosity, for galaxies at $z = 0.0$, $z = 1.2$, and $z = 2.0$. Observations at $z = 0.0$ are from Malhotra et al. (2001) and de Looze et al. (2011).

3.4 [C II] (158 μm) and [O I] (63 μm) cooling lines

[O I] (63 μm) and [C II] (158 μm) are the two dominant cooling lines for interstellar gas. [C II] (158 μm) is considered to be a potentially promising indicator of a galaxy's SFR (e.g. de Looze et al. 2011). In Fig. 11 (left panel) we present the [C II] luminosity of our galaxies as a function of their FIR luminosity. Observations are taken from Malhotra et al. (2001) and de Looze et al. (2011). We note that the authors apply different approaches in estimating the total FIR luminosity. The Malhotra et al. (2001) FIR estimates only cover a wavelength range from 40 to 500 μm, whereas our and the de Looze et al. (2011) FIR luminosities cover a wider wavelength range. We therefore expect the modelled galaxies to be more FIR luminous compared to the sample presented in Malhotra et al. (2001). We find decent agreement with the observations over the entire range of FIR luminosities constrained by observations. The [C II] luminosity of galaxies at $z = 1.2$ and $z = 2.0$ has a minor offset towards lower values compared with the predicted luminosity of local galaxies. This is again driven by a higher SFE in galaxies at high redshift (see Section 4).

Whereas [C II] (158 μm) acts as an important coolant in the diffuse medium, [O I] (63 μm) cooling dominates in denser environments with densities above a few times 10^3 cm^{-3}. Our model predicts an increase in [O I] (63 μm) luminosity with FIR luminosity (Fig. 11, right panel). We overpredict the [O I] luminosity of observed local galaxies, and the predicted slope is steeper than suggested by observations (Malhotra et al. 2001). The predicted [O I] luminosity in high-redshift galaxies is very similar to the [O I] luminosities in local galaxies.

These results are encouraging, as they imply that we correctly model and reproduce the [C II] (158 μm) cooling line in local galaxies from more diffuse regions. We look forward to being able to compare our results with luminosities of statistical sets of typical star-forming galaxies at high redshift. We discuss the contribution from [C II] and [O I] to the cooling of the cold gas in the next section.

3.5 Cooling

In this subsection we discuss the dominant cooling processes acting in the modelled galaxies. The net cooling rate and the dominant coolant of a galaxy all depend heavily on the physical state of the cold gas. The relative contribution of each coolant is therefore yet another diagnostic to study the properties of the star-forming cold gas.

We present the cooling contribution of each individual CO excitation line (CO-to-FIR luminosity ratio) in the form of SLEDs in Fig. 12, separated into bins of FIR luminosity. Our results are compared with observations taken from Narayanan et al. (2005), Lisenfeld et al. (2011), and Papadopoulos et al. (2012). The more FIR-luminous a galaxy, the more important the cooling through higher-J CO lines becomes. Cooling through CO $J = 4 - 3$ and higher is especially dependent on the FIR luminosity. This is tightly connected to the peaks in excitation level as predicted by our model (see Fig. 4), where we also saw that more FIR-luminous galaxies peak at higher excitation levels. These results suggest that in more luminous galaxies most of the cooling takes place in denser regions, traced by CO $J = 5 - 4$ and higher.

Cooling through CO is approximately as efficient at high redshifts as it is in local galaxies for the low-FIR brightness galaxies in our sample ($L_{FIR} < 10^{10}$ L$_\odot$). Cooling through CO becomes less efficient with increasing redshift for the more FIR luminous galaxies in our sample. The dominant cooling occurs through higher CO J-states with increasing redshift, independent of the FIR brightness of a galaxy. For example, at $z = 0.0$ the cooling curve for galaxies with an FIR luminosity of $9.0 < \log (L_{FIR}/L_\odot) < 9.5$ peaks at CO $J = 4 - 3$, whereas it peaks at CO $J = 5 - 4$ and $J = 6 - 5$ in galaxies at $z = 1.2$ and $z = 2.0$, respectively. Dominant CO cooling changes from the $J = 6 - 5$ state at $z = 0.0$ to the $J = 7 - 6$ state at $z = 2.0$ for galaxies with FIR brightnesses $10.0 < \log (L_{FIR}/L_\odot) < 10.5$. These results suggest that the cooling takes place in denser regions, in good agreement with the CO SLED presented in Fig. 4.

We present the cooling rates of carbon, ionized carbon and oxygen in Fig. 13. The cooling rate of all of these chemical species is relatively constant with increasing FIR luminosity, both in low- and in high-redshift galaxies. We find a small decrease in the cooling rate of [C II] for galaxies brighter than $\log (L_{FIR}/L_\odot) > 10$. This resembles the [C II]–FIR deficit in galaxies, in which the [C II]/FIR ratio of galaxies goes down with increasing FIR brightness (see Casey, Narayanan & Cooray 2014, and references therein for a review); however, we do not see this trend for galaxies with FIR
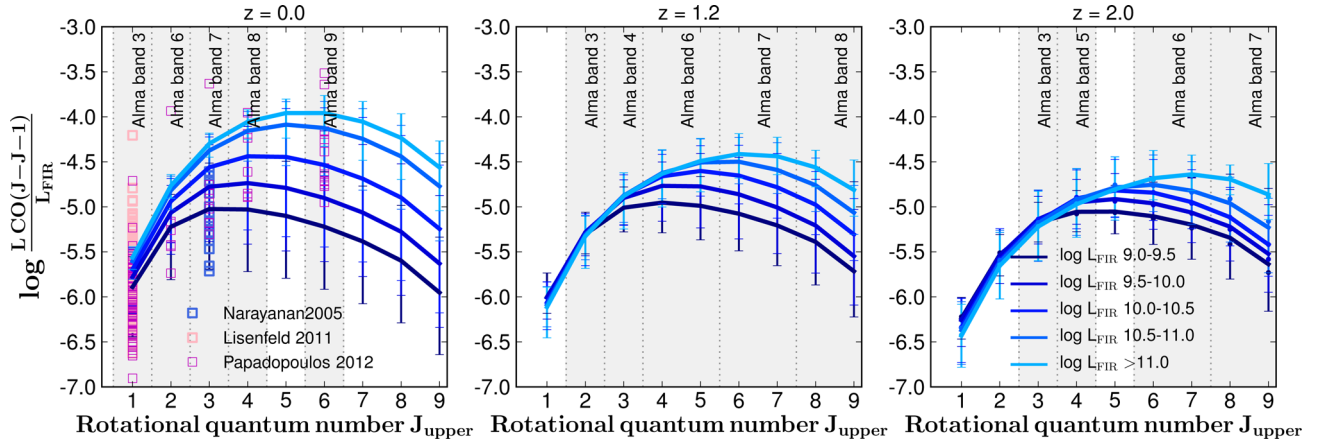
Figure 12. CO $J = J - (J - 1)$ to FIR luminosity ratio as a function of J level, separated in bins of FIR luminosity at redshifts $z = 0.0$ (left panel) and $z = 1.2$ (middle panel) and $z = 2.0$ (right panel). The CO $J = J - (J - 1)$ to FIR luminosity ratio represents the cooling of the molecular gas through a CO line. Observations at $z = 0.0$ are from Narayanan et al. (2005), Lisenfeld et al. (2011), and Papadopoulos et al. (2012).
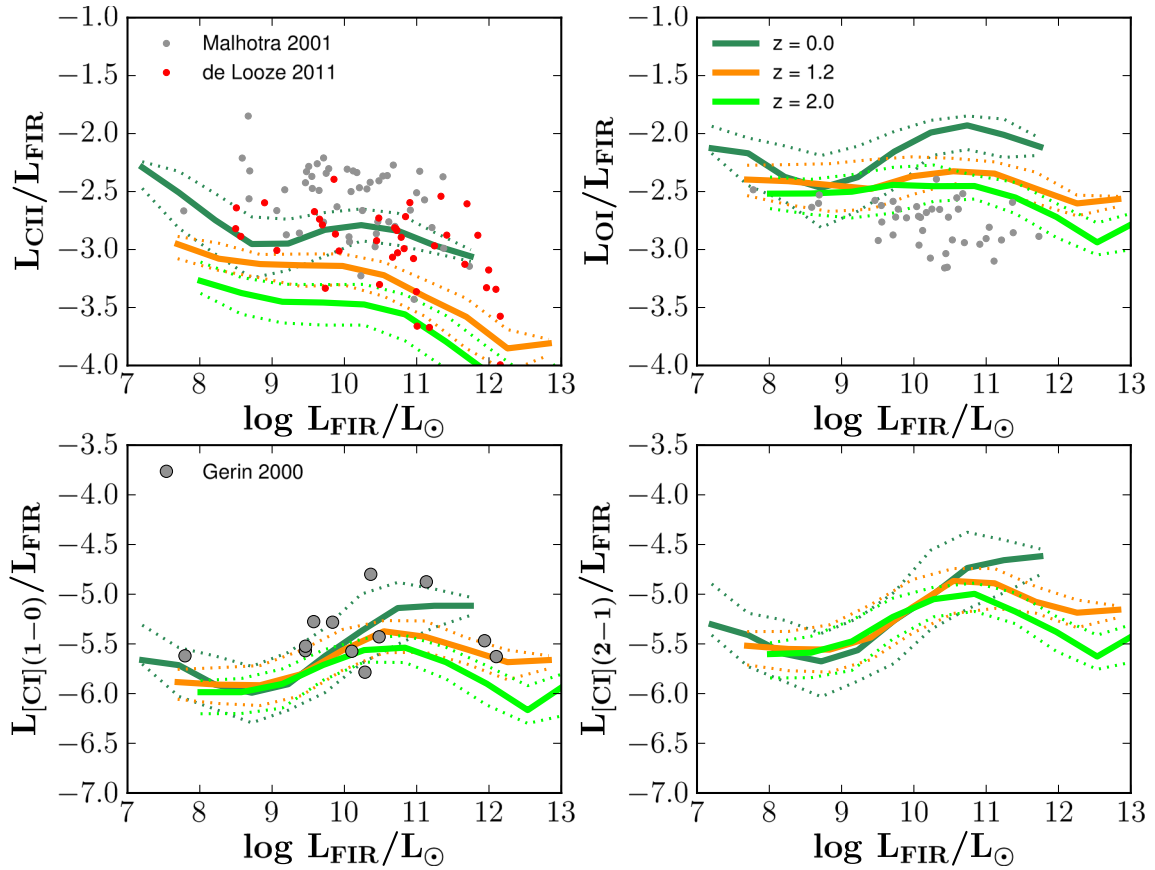

Figure 13. Ratio of CI(1–0), CI(2–1), [C II] (158 μm), and [O I] (63 μm) luminosity to FIR luminosity as a function of FIR luminosity at redshifts $z = 0.0$, $z = 1.2$, and $z = 2.0$. Observations are from Gerin & Phillips (2000), Malhotra et al. (2001), and de Looze et al. (2011).

luminosities fainter than 10^{10} L$_\odot$. At $z = 1.2$ and $z = 2.0$ the [C II]–FIR deficit is prominent over the entire range in FIR luminosities probed. The contribution to the cooling budget from oxygen, carbon and CO stays constant or even increases in this FIR luminosity range. This suggests that the ionized carbon column saturates and cooling takes place through other atomic and molecular species. We see that [C II] and [O I] are the dominant coolants for the neutral gas, whereas the contribution to the total cooling by neutral carbon

is approximately two orders of magnitude weaker at $z = 0$. The contribution to the total cooling by atomic carbon is even more negligible at $z = 1.2$ and $z = 2.0$. The negligible cooling from neutral carbon with respect to [C II] and [O I] is not only supported by our compilation of observations in the local Universe, but also by observations of SMGs at $z > 2.0$ (Walter et al. 2011). CI (2–1) contributes slightly more to the total cooling budget than CI (1–0), albeit still significantly less than [C II] and [O I].
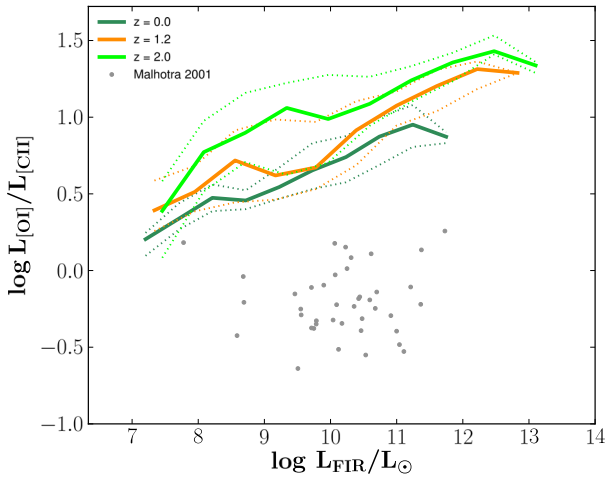
Figure 14. The ratio between the [O I] (63 μm) and [C II] (158 μm) fine-structure lines as a function of FIR luminosity. This ratio traces the relative contribution to the cooling from dense ([O I], densities larger than $\sim 10^4\,\mathrm{cm}^{-3}$) and more diffuse ([C II], lower densities) regions. Observations are from Malhotra et al. (2001).

Adding up all the cooling rates we find that carbon contributes less than one per cent to the total cooling in the modelled galaxies. Cooling through [C II] and [O I] dominates the total cooling budget up to FIR luminosities of $10^{10.5}\,\mathrm{L}_\odot$. The contribution to the total cooling budget by CO increases at higher FIR luminosities, up to roughly 50 per cent in the galaxies with brightest FIR luminosities. This trend is independent of redshift.

Cooling through [C II] is approximately a dex lower in galaxies at $z = 1.2$ and $z = 2.0$, whereas cooling through [O I] decreases with only 0.5 dex. We present the ratio between [O I] and [C II] cooling in Fig. 14. This ratio gives clear insight into which coolant becomes more dominant at the redshifts probed and as a function of FIR luminosity. We see an increase in [O I]/[C II] with increasing FIR luminosity in galaxies at $z = 0.0$, indicative of a more dominant role of cooling through [O I]. The [O I]/[C II] ratio in galaxies at high redshift is ~ 0.5 dex higher than in local galaxies, independent of FIR luminosity. A larger fraction of dense and warm molecular clouds accounts for the more dominant contribution of [O I] to the cooling.

4 DISCUSSION

In this paper we have presented a new set of theoretical models to predict the sub-mm line emission properties of galaxies. Our approach combines a semi-analytic galaxy formation model that explicitly tracks the amount of gas in an atomic and molecular phase (Popping et al. 2014, Somerville, Popping & Trager in preparation) with a fully three-dimensional radiative-transfer and non-local escape probability line tracing code (Poelman & Spaans 2006; Pérez-Beaupuits et al. 2011). This approach provides sub-mm velocity maps, spectra and integrated luminosities of mock galaxies. This model can provide detailed predictions of ISM properties for statistical samples of galaxies that can be directly compared with upcoming observations from ALMA, PdBI, LMT. Furthermore, it drastically increases the number of predicted observables to be constrained by current and future observations. We did not include the effects from AGN and shocks, which could add extra radiative or mechanical energy to the system, heating up the gas. These

processes do have the ability to enhance the emission from high J-transition lines. Because we limit ourselves to average galaxies on the star-forming 'main sequence', we do not expect these processes to be of significant importance for this work.

We use our newly developed model to study the ISM properties in typical star-forming galaxies at $z = 2.0$, $z = 1.2$, and $z = 0$. We aim to understand, from the model's perspective, if the physical state of the gas in typical star-forming galaxies during the peak of the SF history of the Universe, is similar to local counterparts or if the ISM physics that drives the SF is significantly different.

We find that our approach is capable of reproducing sub-mm line luminosity observations in both local and high-z galaxies. We correctly predict the emission arising from CO, [C I], and [C II] at both low and high redshift. These lines trace different regimes, ranging from diffuse media with densities of the order of $\sim 10^3$–$10^4\,\mathrm{cm}^{-3}$ to dense cores with densities of $10^6\,\mathrm{cm}^{-3}$. Furthermore, they arise in both atomic and molecular regions of the ISM. It is encouraging to see that our approach is successful in reproducing these different states of the ISM in galaxies. Unfortunately, to date, the sub-mm emission from typical star-forming galaxies at high redshift is not well constrained by observations. We believe that the predictive power of our model can be valuable for future surveys with ALMA and other sub-mm telescopes, but we also look forward to use such surveys to better constrain our models.

We acknowledge that our models do not reach the necessary resolution to self-consistently model the different phases of the ISM (which is the case for all existing models of galaxy formation in a cosmological context). We adopt simple assumptions about the distribution of the ISM structure within a grid cell. Nevertheless, these simple assumptions tell us something about the structure of the ISM. We find that a LN density distribution for the cold gas within a galaxy is very appropriate to reproduce observations of the sub-mm emission in local and distant galaxies covering a large range of densities probed.

Despite the success of our approach we underpredict the HCN luminosity of galaxies at $z = 0$ by a factor of 3 (see Figs 7 and 8). HCN has critical densities of $10^6\,\mathrm{cm}^{-3}$ and higher, indicative that there are not sufficient molecular clouds in the model galaxies that have the core densities required to reproduce the observations. A remedy would require large gas reservoirs, a higher cold gas surface density, or a larger fraction of dense cores in the molecular clouds. The first two come with the risk of predicting too high gas masses, SFRs and molecular fractions: properties that are reproduced correctly by the current version of the SAM for local and high-redshift observations (Popping et al. 2014). A larger number of dense cores would be a more subtle solution but requires a slight revision of the LN approach adopted in this work.

Our model does not correctly reproduce the slope and normalization of the observed relation between [O I] and FIR luminosity. The over-predicted [O I] luminosity could be due to an over-estimate of the oxygen abundance by our models due to a not yet well understood or implemented oxygen chemistry. This oxygen chemistry should consider a larger fraction of the oxygen budget being depleted into dust grains in the form of major oxygen bearing molecules, such as H_2O and O_2. This is the same problem as found between models and observations of Galactic molecular clouds, where the observed abundance of H_2O and O_2 molecules is at least one order of magnitude lower than expected from current chemical models (e.g. van Dishoeck et al. 1993; Spaans & van Dishoeck 2001; Goldsmith et al. 2011; Liseau et al. 2012). Hence, we should consider, in a future work, a scenario where a significant fraction

of the oxygen budget is lost into icy mantles of dust grains in high column density ($N(H_2) > 10^{22}$ cm^{-2}) clouds.

At fixed redshift the CO SLED of FIR-luminous galaxies peaks at higher excitation levels than in less FIR-luminous galaxies (Fig. 4). Similarly, CO line ratios increase as a function of the SFR in galaxies and the cooling through molecular lines occurs in higher-J CO levels in more FIR bright galaxies. These trends may partially be driven by a low CO abundance in the galaxies with lowest metallicities. Above FIR luminosities of $10^{9-9.5}$ L$_\odot$ the cold gas in galaxies is equally enriched in CO. Furthermore, the [O I]/[C II] cooling-line ratio increases with FIR luminosity. These results indicate that FIR-luminous galaxies are being built up by warmer and denser molecular clouds than less-bright galaxies.

We briefly studied the behaviour of the CO-to-H$_2$ conversion factor α_{CO}. We find good agreement with observations of α_{CO} for galaxies over a large range of metallicities. We predict a steep decline in α_{CO} at the lowest metallicities $Z' < 0.1$ and a flat distribution of α_{CO} at higher metallicities. These results are consistent with other theoretical results (Feldmann et al. 2012; Narayanan et al. 2012) and are mostly driven by the low CO abundance of low-metallicity gas. The approach presented in this work is still somewhat over-simplified. A detailed study of α_{CO} should include a proper chemical network, simultaneously solving for the CO abundance and H$_2$ abundance of cold gas as a function of density, optical depth, impinging radiation field and individual elemental abundances. This is a computationally expensive exercise, and beyond the scope of this work.

The carbon excitation temperature in galaxies at $z = 1.2$ and $z = 2.0$ is warmer (approximately 10 K) than in galaxies at $z = 0$. This is suggestive of a warmer atomic ISM in star-forming galaxies at high redshift. Our predicted atomic ISM temperatures are in good agreement with results from Weiß et al. (2005) and Walter et al. (2011), who found that the carbon excitation temperature in SMGs at $z > 2.0$ is around 30 K. Furthermore, the carbon-to-CO ratio also is constant with redshift, demonstrating that the carbon and CO $J = 1 - 0$ emission arise in roughly the same medium. Neutral carbon provides only a negligible contribution to the total cooling in a galaxy.

We have compared the sub-mm line properties of modelled galaxies at $z = 0.0$, $z = 1.2$, and $z = 2.0$ in some detail, with the aim of understanding whether the gas properties of galaxies at high redshift are different from local counterparts. Within the models, we find multiple examples of evidence that suggest that SF in galaxies during the SF activity peak of the Universe takes place in much denser and warmer environments than SF in similar galaxies at $z = 0$. Galaxies at high redshift show a peak in their CO SLED at higher CO J-states (Fig. 4), have higher CO $J = 5 - 4$/CO $J = 2 - 1$ and CO $J = 7 - 6$/CO $J = 2 - 1$ ratios as a function of several global galaxy properties (Fig. 5). Furthermore, cooling through the [O I] 63 µm fine structure line becomes more dominant and molecular cooling occurs through higher J CO levels. All these results are indicative of a difference in gas density and temperature between typical star-forming galaxies in the local Universe and at high redshift. Rather than being in a similar physical state as local galaxies, the cold gas in typical star-forming galaxies at high redshift appears to have different physical properties. We find that galaxies at $z = 1.2$ have lower excitation temperatures and densities than similar galaxies at $z = 2.0$. This indicates that different ISM conditions are already visible right after the actual SF peak of the Universe ($z < 2.0$).

The CO line ratios of galaxies remain constant with time when plotted as a function of H$_2$ surface density. Although the shape of the CO SLED is determined by a number of quantities such as density, turbulence and temperature, this suggests that we can describe the CO SLED to first order as a function of only the H$_2$ surface density. One should keep in mind that within our model the SFR of a galaxy (which will ultimately set the cold gas temperature) is a function of H$_2$ surface density as well. We therefore believe our results are also in good agreement with the work by Narayanan & Krumholz (2014), who found that the CO SLED of a galaxy is well correlated with a galaxy's SFR surface density.

Our results provide an explanation for the shorter depletion times observed in galaxies at high redshift (Genzel et al. 2010). The higher densities will shorten the free-fall time of the molecular clouds, and thus enhance the rate at which gas may condense and form stars. This increment in SFE provides an attractive way to increase the SFR density of the Universe. A denser medium allows less gas-rich galaxies to contribute to the total SFR more efficiently than less dense objects with similar SFR, but driven by lower density (and more) gas. This behaviour is reflected in our models through the lower luminosities from low J-states of CO, HCN, [C I] and [C II] in galaxies at $z = 1.2$ and $z = 2.0$ compared to local galaxies. There are effectively fewer atoms and molecules that can add to the galaxy's emission for the same net amount of FIR radiation. The available observations for high-redshift galaxies do not convincingly support such a trend (Tacconi et al. 2010, 2013). It is currently premature to draw a firm conclusion on this point, given the small sample size and strong bias towards extreme SF of the present observations.

Observationally, the difference in ISM properties between local and high-redshift galaxies is not well constrained. Dannerbauer et al. (2009) suggest that the star-forming conditions in a typical star-forming galaxy are similar to local galaxies. These observations, however, only go out to CO $J = 3 - 2$ and do not probe the CO excitation levels where our models show a clear difference between local and high-redshift galaxies. Furthermore, their conclusion is based on only two galaxies. We hope that future observations of (parts of) the CO SLED with ALMA will better constrain the gas properties of typical star-forming galaxies at high redshifts.

A first attempt at combining semi-analytic models of galaxy formation with radiative-transfer codes was presented in Lagos et al. (2012). The authors parametrize modelled galaxies with a single cold gas density, UV radiation field, metallicity and X-ray intensity and use a library of pre-calculated radiative-transfer models to infer conversion factors between H$_2$ mass and CO line-intensities. The authors find similar trends with FIR luminosity for the luminosity from low excitation CO lines as we do. We predict higher luminosities and a larger contribution to the molecular cooling from high J CO lines ($J = 5 - 4$ and up) compared with their results. We ascribe this difference to their representation of a galaxy with a single non-variable ISM density of 10^4 cm^{-3} (although see their section 5 for a discussion about using different densities). In our approach galaxies are represented by the summation of multiple molecular clouds with varying density. This becomes especially relevant for CO lines like $J = 5 - 4$ and up, as the critical densities of these lines lie almost an order of magnitude above 10^4 cm^{-3}, if not more. Lagos et al. (2012) only study the CO luminosities of their modelled galaxies, and do not present predictions for emission from other atomic and molecular species. We have shown that the ability to examine more atomic and molecular species provides a more detailed picture of the ISM and its different phases.

5 SUMMARY

In this paper we developed new models of the sub-mm line emission from atomic and molecular species for statistical sets of galaxies. We summarize our main findings below:

(i) We successfully reproduce observed scaling relations for the line luminosities emitted by CO, C, C^+, and O for nearby galaxies. These atomic and molecular species trace a wide range in molecular cloud properties (gas temperatures and densities), indicating that our model correctly reproduces the multi-phase structure of molecular clouds.

(ii) The peak excitation level of the CO SLED in modelled galaxies increases with FIR luminosity, as well as with redshift.

(iii) CO line ratios of our modelled galaxies show a clear increasing trend with global SF tracing properties (SFR, FIR luminosity, cold gas surface density) and with redshift (SFR, FIR luminosity). Most notable changes in CO line ratios are achieved when using CO $J = 5 - 4$/CO $J = 2 - 1$ and higher. These are lines that ALMA can potentially observe at $z > 1.0$. The CO line ratios of galaxies are well correlated with galaxy H_2 surface density independent of redshift.

(iv) Galaxies at $z = 1.2$ and $z = 2.0$ have weaker low-J line luminosities of CO, HCN, and [C I] than galaxies at $z = 0.0$ with similar SFR and FIR luminosity.

(v) The atomic gas properties of galaxies, as traced through neutral carbon, in local galaxies and galaxies at high redshift, are similar, with no notable difference in carbon excitation temperature.

(vi) The [O I]/[C II] cooling line ratio is higher in galaxies at high redshift than in local galaxies, suggesting that cooling predominantly takes place in denser regions.

(vii) Our model results indicate that SF in galaxies at high redshift takes place in denser and warmer environments than in local counterparts. This suggests that SF during the peak of the SF activity in the Universe is not driven by gas in a similar physical state as in local galaxies, but by significantly different ISM conditions. Galaxies belonging to the tail of the SF activity peak of the Universe ($z = 1.2$) are already less dense and cooler than counterparts during the actual peak of SF activity ($z = 2.0$).

Observations with the current and next generation of sub-mm telescopes such as ALMA, LMT, and PdBI will allow us to test the predictions made in this work for large samples of galaxies. Not only can these observations be placed in their proper physical context using models as presented in this work, they will also further constrain models of galaxy formation and evolution. Most notable results can be obtained by observing line ratios of CO in high- and low-J states (tracing a critical density difference of at least an order of magnitude). Not only will observations of tracers of such different gas phases give insight into the dominant gas distribution, they also provide strong constraints on the CO SLED from which density and excitation temperatures can be derived. Besides CO emission, atomic cooling lines [O I] 63 μm and [C II] 158 μm also provide great potential to study ISM properties in galaxies. We predict a difference in [O I]/[C II] ratios with redshift, directly related to the density and temperature of the ISM.

Our approach, in combination with future surveys, holds great potential for further understanding galaxy formation. It allows us to constrain not only the amount of cold gas in galaxies, but also the actual density and temperature distribution of the gas that will set the rate of formation of stars and the build-up of stellar discs. Any physical process that acts on the cold gas content of a galaxy should result in a temperature and density distribution and line emission along the atomic and/or molecular energy ladder in close agreement with observations. Comparing sub-mm observations across cosmic time with our model therefore provides an attractive way to constrain the physics acting on the cold gas that account for the gas content and SF activity in galaxies during the peak of SF in the Universe and its turnover at lower redshifts. [C II] luminosities will be a powerful way of constraining model predicted SFRs in the high-redshift Universe. Furthermore, when including the spatial and velocity information, we are in the position to make predictions for observed CO disc sizes and velocities. This offers the unique possibility to address the topic of disc angular momentum at redshifts above $z = 0$.

REFERENCES

Arrigoni M., Trager S. C., Somerville R. S., Gibson B. K., 2010, MNRAS, 402, 173
Bauermeister A. et al., 2013, ApJ, 768, 132
Bayet E., Gerin M., Phillips T. G., Contursi A., 2004, A&A, 427, 45
Berry M., Somerville R. S., Haas M. R., Gawiser E., Maller A., Popping G., Trager S. C., 2014, MNRAS, 441, 939
Bigiel F., Leroy A., Walter F., Brinks E., de Blok W. J. G., Madore B., Thornley M. D., 2008, AJ, 136, 2846
Blumenthal G. R., Faber S. M., Flores R., Primack J. R., 1986, ApJ, 301, 27
Bolatto A. D., Leroy A. K., Rosolowsky E., Walter F., Blitz L., 2008, ApJ, 686, 948
Carilli C. L., Walter F., 2013, ARA&A, 51, 105
Casey C. M., Narayanan D., Cooray A., 2014, preprint (arXiv 1402.1456)
Christensen C., Quinn T., Governato F., Stilp A., Shen S., Wadsley J., 2012, MNRAS, 425, 3058
Daddi E. et al., 2010, ApJ, 713, 686
Danielson A. L. R. et al., 2011, MNRAS, 410, 1687
Dannerbauer H., Daddi E., Riechers D. A., Walter F., Carilli C. L., Dickinson M., Elbaz D., Morrison G. E., 2009, ApJ, 698, L178
de Looze I., Baes M., Bendo G. J., Cortese L., Fritz J., 2011, MNRAS, 416, 2712
Draine B. T., Bertoldi F., 1996, ApJ, 468, 269
Feldmann R., Gnedin N. Y., Kravtsov A. V., 2012, ApJ, 747, 124
Fixsen D. J., Bennett C. L., Mather J. C., 1999, ApJ, 526, 207
Flores R., Primack J. R., Blumenthal G. R., Faber S. M., 1993, ApJ, 412, 443
Fu J., Guo Q., Kauffmann G., Krumholz M. R., 2010, MNRAS, 409, 515
Fu J., Kauffmann G., Li C., Guo Q., 2012, MNRAS, 424, 2701
Gao Y., Solomon P. M., 2004, ApJ, 606, 271
Gao Y., Carilli C. L., Solomon P. M., Vanden Bout P. A., 2007, ApJ, 660, L93
Geach J. E., Smail I., Moran S. M., MacArthur L. A., Lagos C. d. P., Edge A. C., 2011, ApJ, 730, L19
Genzel R. et al., 2010, MNRAS, 407, 2091
Genzel R. et al., 2012, ApJ, 746, 69
Gerin M., Phillips T. G., 2000, ApJ, 537, 644
Giavalisco M. et al., 2004, ApJ, 600, L93
Gnedin N. Y., Kravtsov A. V., 2011, ApJ, 728, 88
Gnedin N. Y., Tassis K., Kravtsov A. V., 2009, ApJ, 697, 55
Goldsmith P. F. et al., 2011, ApJ, 737, 96
Grogin N. A. et al., 2011, ApJS, 197, 35

Helfer T. T., Thornley M. D., Regan M. W., Wong T., Sheth K., Vogel S. N., Blitz L., Bock D., 2003, ApJS, 145, 259
Hennebelle P., Chabrier G., 2008, ApJ, 684, 395
Hennebelle P., Chabrier G., 2009, ApJ, 702, 1428
Hollenbach D. J., Takahashi T., Tielens A. G. G. M., 1991, ApJ, 377, 192
Hopkins A. M., Beacom J. F., 2006, ApJ, 651, 142
Israel F. P., Baas F., 2001, A&A, 371, 433
Israel F. P., Baas F., 2002, A&A, 383, 82
Israel F. P., Baas F., 2003, A&A, 404, 495
Israel F. P., Tilanus R. P. J., Baas F., 2006, A&A, 445, 907
Juneau S., Narayanan D. T., Moustakas J., Shirley Y. L., Bussmann R. S., Kennicutt R. C., Jr, Vanden Bout P. A., 2009, ApJ, 707, 1217
Koekemoer A. M. et al., 2011, ApJS, 197, 36
Komatsu E. et al., 2009, ApJS, 180, 330
Kravtsov A. V., 1999, PhD thesis, New Mexico State University
Krumholz M. R., Dekel A., 2012, ApJ, 753, 16
Krumholz M. R., McKee C. F., 2005, ApJ, 630, 250
Kuhlen M., Krumholz M. R., Madau P., Smith B. D., Wise J., 2012, ApJ, 749, 36
Lagos C. D. P., Baugh C. M., Lacey C. G., Benson A. J., Kim H.-S., Power C., 2011a, MNRAS, 1776
Lagos C. D. P., Lacey C. G., Baugh C. M., Bower R. G., Benson A. J., 2011b, MNRAS, 416, 1566
Lagos C. d. P., Bayet E., Baugh C. M., Lacey C. G., Bell T. A., Fanidakis N., Geach J. E., 2012, MNRAS, 426, 2142
Larson R. B., 1981, MNRAS, 194, 809
Lemaster M. N., Stone J. M., 2008, ApJ, 682, L97
Leroy A. K., Walter F., Brinks E., Bigiel F., de Blok W. J. G., Madore B., Thornley M. D., 2008, AJ, 136, 2782
Leroy A. K. et al., 2011, ApJ, 737, 12
Liseau R. et al., 2012, A&A, 541, A73
Lisenfeld U. et al., 2011, A&A, 534, A102
Loenen A. F., Spaans M., Baan W. A., Meijerink R., 2008, A&A, 488, L5
Malhotra S. et al., 2001, ApJ, 561, 766
Meijerink R., Spaans M., 2005, A&A, 436, 397
Meijerink R., Spaans M., Israel F. P., 2006, ApJ, 650, L103
Meijerink R., Spaans M., Israel F. P., 2007, A&A, 461, 793
Mo H. J., Mao S., White S. D. M., 1998, MNRAS, 295, 319
Murray N., Rahman M., 2010, ApJ, 709, 424
Narayanan D., Krumholz M., 2014, MNRAS, 442, 1411
Narayanan D., Groppi C. E., Kulesa C. A., Walker C. K., 2005, ApJ, 630, 269
Narayanan D. et al., 2008, ApJS, 176, 331
Narayanan D., Krumholz M. R., Ostriker E. C., Hernquist L., 2012, MNRAS, 421, 3127
Navarro J. F., Frenk C. S., White S. D. M., 1996, ApJ, 462, 563
Obreschkow D., Croton D., De Lucia G., Khochfar S., Rawlings S., 2009, ApJ, 698, 1467

Ojha R. et al., 2001, ApJ, 548, 253
Oka T. et al., 2005, ApJ, 623, 889
Ostriker E. C., Stone J. M., Gammie C. F., 2001, ApJ, 546, 980
Papadopoulos P. P., van der Werf P. P., Xilouris E. M., Isaak K. G., Gao Y., Mühle S., 2012, MNRAS, 426, 2601
Pelupessy F. I., Papadopoulos P. P., van der Werf P., 2006, ApJ, 645, 1024
Pérez-Beaupuits J. P., Wada K., Spaans M., 2011, ApJ, 730, 48
Plummer H. C., 1911, MNRAS, 71, 460
Poelman D. R., Spaans M., 2005, A&A, 440, 559
Poelman D. R., Spaans M., 2006, A&A, 453, 615
Popping G., Caputi K. I., Somerville R. S., Trager S. C., 2012, MNRAS, 425, 2386
Popping G., Somerville R. S., Trager S. C., 2014, MNRAS, 442, 2398
Price D. J., Federrath C., Brunt C. M., 2011, ApJ, 727, L21
Robertson B. E., Kravtsov A. V., 2008, ApJ, 680, 1083
Robitaille T. P., Whitney B. A., 2010, ApJ, 710, L11
Sandstrom K. M. et al., 2013, ApJ, 777, 5
Schöier F. L., van der Tak F. F. S., van Dishoeck E. F., Black J. H., 2005, A&A, 432, 369
Schruba A. et al., 2011, AJ, 142, 37
Scoville N. et al., 2007, ApJS, 172, 1
Shostak G. S., van der Kruit P. C., 1984, A&A, 132, 20
Somerville R. S. et al., 2008a, ApJ, 672, 776
Somerville R. S., Hopkins P. F., Cox T. J., Robertson B. E., Hernquist L., 2008b, MNRAS, 391, 481
Somerville R. S., Gilmore R. C., Primack J. R., Domínguez A., 2012, MNRAS, 423, 1992
Spaans M., van Dishoeck E. F., 2001, ApJ, 548, L217
Stutzki J. et al., 1997, ApJ, 477, L33
Tacconi L. J. et al., 2010, Nature, 463, 781
Tacconi L. J. et al., 2013, ApJ, 768, 74
Tielens A. G. G. M., 2005, The Physics and Chemistry of the Interstellar Medium. Cambridge Univ. Press, Cambridge
van der Tak F. F. S., Black J. H., Schöier F. L., Jansen D. J., van Dishoeck E. F., 2007, A&A, 468, 627
van Dishoeck E. F., Blake G. A., Draine B. T., Lunine J. I., 1993, in Levy E. H., Lunine J. I., eds, Protostars and Planets III. p. 163
Wada K., Norman C. A., 1999, ApJ, 516, L13
Wada K., Norman C. A., 2007, ApJ, 660, 276
Wada K., Papadopoulos P. P., Spaans M., 2009, ApJ, 702, 63
Walter F., Weiß A., Downes D., Decarli R., Henkel C., 2011, ApJ, 730, 18
Weiß A., Walter F., Scoville N. Z., 2005, A&A, 438, 533
Wolfire M. G., Hollenbach D., McKee C. F., 2010, ApJ, 716, 1191

This paper has been typeset from a TeX/LaTeX file prepared by the author.